CRISPR screens reveal genetic determinants of PARP inhibitor sensitivity and resistance in prostate cancer

Takuya Tsujino[1,2,11], Tomoaki Takai[1,2,11], Kunihiko Hinohara[3,4,11], Fu Gui[1], Takeshi Tsutsumi[1,2], Xiao Bai[1], Chenkui Miao[1], Chao Feng[1], Bin Gui[1], Zsofia Sztupinszki[5,6], Antoine Simoneau[7], Ning Xie[8], Ladan Fazli[8], Xuesen Dong[8,9], Haruhito Azuma[2], Atish D. Choudhury[3], Kent W. Mouw[10], Zoltan Szallasi[5,6], Lee Zou[7], Adam S. Kibel[1], Li Jia[1, *]

[1]Division of Urology, Department of Surgery, Brigham and Women's Hospital & Harvard Medical School, Boston, MA, USA

[2]Department of Urology, Osaka Medical and Pharmaceutical University, Osaka, Japan

[3]Department of Medical Oncology, Dana-Farber Cancer Institute & Harvard Medical School, Boston, MA, USA

[4]Department of Immunology, Nagoya University Graduate School of Medicine, Nagoya, Japan

[5]Computational Health Informatics Program, Boston Children's Hospital, Boston, MA, USA

[6]Danish Cancer Society Research Center, Copenhagen, Denmark

[7]Department of Pathology, Massachusetts General Hospital & Harvard Medical School, Boston, MA, USA

[8]Vancouver Prostate Centre, Vancouver General Hospital, Vancouver, British Columbia, Canada

[9]Department of Urologic Sciences, University of British Columbia, Vancouver, British Columbia, Canada

[10]Department of Radiation Oncology, Dana-Farber Cancer Institute & Brigham and Women's Hospital & Harvard Medical School, Boston, MA, USA

[11]These authors contributed equally to this article.

* Correspondence author: ljia@bwh.harvard.edu

ABSTRACT

Prostate cancer (PCa) harboring BRCA1/2 mutations is often exquisitely sensitive to PARP inhibition. However, genomic alterations in other DNA damage response genes have not been consistently predictive of clinical response to PARP inhibitors (PARPis). Here, we perform genome-wide CRISPR-Cas9 knockout screens in BRCA1/2-proficient PCa cell lines and identify novel genes whose loss has a profound impact on PARPi sensitivity and resistance. Specifically, MMS22L deletion, frequently observed (up to 14%) in PCa, renders cells hypersensitive to PARPis by disrupting RAD51 loading required for homologous recombination repair, although this response is TP53-dependent. Unexpectedly, loss of CHEK2 confers resistance rather than sensitivity to PARPis in PCa cells through increased expression of BRCA2, a target of CHEK2-TP53-E2F7-mediated transcriptional repression. Combined PARP and ATR inhibition overcomes PARPi resistance caused by CHEK2 loss. Our findings may inform the use of PARPis beyond BRCA1/2-deficient tumors and support reevaluation of currently used biomarkers for PARPi treatment in PCa.

43 **INTRODUCTION**

44 Despite treatment advances, metastatic castration-resistant prostate cancer (mCRPC)
45 remains a lethal disease. Genomic sequencing studies reveal that approximately 90% of
46 mCRPC patients carry clinically actionable genomic alterations [1]. Alterations in genes involved
47 in the DNA damage response (DDR) are among the most common genetic events.
48 Approximately 10% of primary and 25% of metastatic PCa patients have an alteration in at least
49 one gene involved in DDR [2], which represents a potential therapeutic vulnerability. In particular,
50 defects in homologous recombination repair (HRR) render cells highly sensitive to inhibition of
51 Poly (ADP-ribose) polymerase (PARP). As a targeted therapy, PARP inhibitors (PARPis)
52 prevent PARP1 and PARP2 from repairing DNA single-strand breaks (SSBs) and leads to
53 stalled and collapsed replication forks by trapping PARP1/2 on the DNA breaks [3]. Subsequently,
54 SSBs are converted to double-strand breaks (DSBs) that HRR-deficient cells cannot repair
55 effectively, leading to overwhelming DNA damage, cell cycle arrest, and cell death. The BRCA1
56 and BRCA2 genes encode proteins essential for HRR, a pathway that repair DNA DSBs.
57 PARPis selectively induce synthetic lethality in cancer cells harboring mutations in the BRCA1/2
58 genes [4,5].

59 Several PARPis are presently under clinical investigation in PCa, including olaparib,
60 rucaparib, niraparib, and talazoparib, as a single agent. Two of them (olaparib and rucaparib)
61 have been approved by the U.S. Food and Drug Administration (FDA) for the treatment of
62 mCRPC patients with deleterious germline and/or somatic mutations in BRCA1/2, and the
63 olaparib indication includes mutations in 12 additional HRR genes [6-11]. It is clear that BRCA1/2-
64 mutant tumors exhibit high sensitivity and improved outcome to PARP inhibition based on
65 results from these trials, as measured by standard radiographic criteria, 50% decrease in
66 prostate-specific antigen (PSA), circulating tumor-cell counts, and progression-free survival or
67 overall survival. However, whether and to what extent PARPis can be used to treat tumors with

68 non-BRCA1/2 alterations remains controversial after gene-by-gene analysis. Furthermore,
69 HRR-deficient tumors are not always sensitive to PARPis. Both intrinsic and acquired resistance
70 to PARP inhibition represents a formidable clinical problem. Therefore, one of the major barriers
71 to effective treatment using PARPis is how to distinguish patients who may and may not benefit
72 from PARP inhibition.

73 The genome-wide CRISPR-Cas9 (clustered regularly interspersed short palindromic repeat-
74 CRISPR associated nuclease 9) knockout (KO) screen is a powerful and unbiased approach to
75 identify genes that, when deleted, confer PARPi sensitivity or resistance. Previous studies using
76 CRISPR screens in non-PCa cell lines have identified genes whose loss impacts PARPi
77 response [12-14]. In this study, we carried out CRISPR screens in four BRCA1/2-proficient PCa cell
78 lines with the goal of expanding the use of PARPis beyond BRCA1/2 mutations and finding new
79 synthetically lethal interactions. Our screens led to the identification of MMS22L, a frequently
80 deleted HRR gene in PCa, as a new predictive biomarker for PARPis. Unexpectedly, we found
81 that loss of CHEK2 caused PARPi resistance, which we explored a therapeutic approach
82 through ATR inhibition to overcome in pre-clinical models.

83 **RESULTS**

84 **Genome-wide CRISPR KO screens identify genes that modulate PARPi response in PCa**
85 **cells.**

86 To identify genes whose loss increases or decreases the sensitivity of PCa cells to PARP
87 inhibition, we performed genome-wide CRISPR KO screens in the PCa LNCaP, C4-2B, 22Rv1
88 and DU145 cells in the presence of olaparib or DMSO vehicle. These four cell lines reflect
89 different aspects of PCa progression to castration resistance and have no deleterious biallelic
90 mutations in BRCA1/2 and other canonical HRR genes determined by whole exome sequencing
91 (Supplementary Table 1). LNCaP and C4-2B cells are relatively more sensitive to olaparib in
92 contrast to 22Rv1 and DU145 cells (Supplementary Fig. 1), but less sensitive when compared

93 to BRCA1-null ovarian cancer UWB1 cells. Cells were transduced with the lentiviral-based
94 CRISPR-Cas9 KO libraries, targeting over 18,000 protein-coding genes as previously described
95 [15,16], followed by 28 days of treatment with olaparib or DMSO (Fig. 1a; Supplementary Fig.
96 2a,b). The abundance of single guide RNA (sgRNA) for each gene was assessed by β-score
97 and the differential β-score was further calculated using the MAGeCKFlute pipeline by
98 comparing olaparib treatment to DMSO treatment [17,18]. We identified 216, 243, 153, and 211
99 negatively selected genes (with a stringent cutoff of *p*-value < 0.01, $\sigma = 2.58$), loss of which
100 sensitizes cells to olaparib in LNCaP, C4-2B, 22Rv1, and DU145 cells, respectively (Fig. 1b;
101 Supplementary Table 2). There were 67 genes shared by at least two cell lines, considered as
102 common hits (Supplementary Table 3). Gene Ontology (GO) analyses revealed that these
103 common hits were enriched for DNA repair and replication functions (Fig. 1c). Further analysis
104 of each individual cell line showed that the mitochondrial complex I assembly was the most
105 enriched function in DU145 (Fig. 1d; Supplementary Fig. 3). Dysfunction of mitochondrial
106 complex I causes a decline of NAD^+ and ATP supply required for PARP-mediated DNA repair [19].
107 The cell-type specific mechanism may provide a unique therapeutic vulnerability.
108 We identified 280, 347, 222, and 281 positively selected genes ($p < 0.01$, $\sigma = 2.58$), loss of
109 which renders cells resistant to olaparib in LNCaP, C4-2B, 22Rv1, and DU145 cells,
110 respectively (Fig. 1e; Supplementary Table 4). Given that cells were cultured in the presence of
111 olaparib for only 28 days, these genes are more likely related to intrinsic resistance rather than
112 acquired resistance arising after prolonged treatment with PARPis. There were 103 genes
113 shared in at least two cell lines (Supplementary Table 5). These common hits were enriched in
114 cell cycle phase transition and positive regulation of transcription (Fig. 1f). Analyses of positively
115 selected genes in each individual cell line showed that cell cycle genes are largely enriched in
116 CRPC C4-2B, 22Rv1, and DU145 cells, but not in androgen-dependent LNCaP cells (Fig. 1d;

117 Supplementary Fig. 3), reflecting the role of cell cycle transition in mediating PARPi resistance
118 in CRPC [20].
119 To further dissect the identified genes implicated in PARPi sensitivity and resistance, we
120 analyzed the common hits using the database in STRING protein-protein association network [21].
121 We found that 50% of the common negatively selected genes could be assigned to well-defined
122 functions in DDR, including HRR, DNA replication, Fanconi anemia, helicase, and cohesion
123 (Fig. 1g). In contrast, approximately 50% of the common positively selected genes were
124 involved specifically in cell cycle, ADP-ribosylation, transcriptional regulation (Fig. 1h). Finally,
125 we ranked all genes based on the average of differential β-scores from all four cell lines.
126 Representative top-ranked negatively and positively selected genes are shown in Fig. 1i,
127 including ones studied in this work. Notably, the BRCA1 and BRCA2 genes were highly ranked
128 in negative selection but reached the cutoff only in C4-2B and DU145 cells, respectively. This is
129 likely because acute inactivation of BRCA1 and BRCA2 is lethal without adaptive mechanisms
130 in cells [22-24], as reflected by the depletion of sgRNAs targeting BRCA1/2 genes even in the
131 absence of olaparib treatment in most cases, thereby failing to reach statistically significant
132 depletion in the olaparib condition (Supplementary Fig. 4). Together, our screen results provide
133 a global view of genetic determinants of PARPi response in PCa.
134 **Validation of negatively selected genes related to PARPi sensitivity.**
135 Next, we examined the alteration frequency (deletion and mutation) of the 67 common
136 negatively selected genes in the TCGA (primary tumors) and SU2C/PCF (metastatic tumors)
137 cohorts (Fig. 2a). We selected ten genes, based on their alteration frequency as well as their
138 important functions in DDR, and individually deleted these genes in C4-2B cells (Supplementary
139 Fig. 5). We observed markedly increased sensitivity to olaparib following deletion (Fig. 2b).
140 Among these genes, HELLS and WDR76 are the only two hits in all four cell lines. HELLS is a
141 helicase and chromatin remodeling enzyme that promotes the initiation of HRR and contributes
142 to DSB repair [25], while WDR76 is a specific reader of 5-hydroxymethylcytosine (5hmC) with

143 uncharacterized functions in DNA repair [26,27]. Indeed, WDR76 has a large interaction network,
144 including HELLS and PARP1 [28], supporting synthetically lethal interaction with PARP inhibition.
145 RNASEH2B and MMS22L are located on chromosomes 13q14 and 6q16, respectively, which
146 are two genomic regions frequently deleted in PCa [29-35]. While loss of RNASEH2B might cause
147 ribonucleotide excision repair deficiency and PARP-trapping lesions as previously reported [13],
148 we recently reported that co-loss of RB1, a closely located tumor suppressor gene, was
149 antagonistic in PCa cells [36]. MMS22L is known to form an obligate heterodimer complex with
150 TONSL, which reads histone H4 unmethylated lysine 20 [37] and promotes HRR of stalled or
151 collapsed replication forks and attendant DSBs by aiding RAD51 loading [38-40]. Cells with
152 MMS22L deletion are highly sensitive to the topoisomerase I inhibitor camptothecin. However,
153 the impact of MMS22L loss on PARP inhibition has not been studied.

154 **Loss of MMS22L increases PARPi response due to impaired HRR function in PCa cells**

155 Since MMS22L always forms a complex with TONSL for replication-associated DNA
156 damage repair, TONSL was unsurprisingly identified as one of the top hits as well (Fig. 1I;
157 Supplementary Table 2). Nevertheless, the frequency of MMS22L homozygous deletions (14%
158 in primary and 5% in metastatic prostate tumors) makes it an attractive biomarker to predict
159 PARPi response in PCa. To further validate this finding, we deleted MMS22L and TONSL in five
160 PCa cell lines - LNCaP, C4-2B, 22Rv1, PC-3, DU145 and MDAPCa2b (Fig. 3a). We showed
161 that deletion of either MMS22L or TONSL resulted in significantly increased sensitivity to
162 olaparib in LNCaP, C4-2B, MDAPCa2b and 22Rv1 cells, but not in DU145 or PC-3 cells. In a
163 growth competition experiment, we observed that olaparib treatment significantly reduced the
164 fraction of MMS22L-KO cells in contrast to corresponding control cells when they were equally
165 pre-mixed and grown under the same treatment condition (Fig. 3b). Notably, MMS22L-deleted
166 C4-2B cells were also sensitive to other PARPis (rucaparib, talazoparib, and veliparib), but
167 displayed lower sensitivity to carboplatin, a DNA crosslinking agent (Fig. 3c). In addition, we
168 generated MMS22L-KO C4-2B cell clones through single cell sorting and confirmed either

169 complete (sg1, clone #1-4) or partial MMS22L deletion (sg1, clone #5-6; sg2, clone #1-6) using
170 immunoblot (Fig. 3d). All MMS22L-KO clones exhibited high sensitivity to olaparib to a similar
171 extent without a gene dose effect, supporting MMS22L haploinsufficiency for its function.
172 Restoration of MMS22L expression completely abolished the sensitivity of MMS22L-KO cells to
173 olaparib (Fig. 3e), confirming that the phenotype was specifically due to MMS22L loss.
174 Next, we sought to investigate the mechanism by which loss of MMS22L increased PARPi
175 sensitivity. We recently reported that PARPi induces replication fork collapse and DSBs in a
176 trans cell cycle manner and BRCA1/2-deficient cells cannot recruit RAD51 to repair them,
177 leading to cell death [20]. Similarly, we observed increased expression of γ-H2AX and cleaved-
178 PARP in MMS22L-KO C4-2B cells following 72h olaparib treatment (Fig. 4a), reflecting PARPi-
179 induced DNA DSBs and apoptosis. Increased γ-H2AX foci were detected by
180 immunofluorescence staining (Fig. 4b). Cell cycle analysis showed a substantial accumulation
181 of cells in G2/M phase after deletion of MMS22L or TONSL (Fig. 4c). Given the function of the
182 MMS22L-TONSL complex in loading RAD51 at DSB sites and promoting HRR after replication
183 fork collapse independent of BRCA2 [38], we postulated that loss of MMS22L might impair HRR
184 that occurred predominantly in the late S and G2 phases of the cell cycle, leading to
185 overwhelming DSBs and mitotic catastrophe. Indeed, using immunofluorescence staining, we
186 found significantly reduced RAD51 foci in MMS22L-KO C4-2B cells after olaparib treatment for
187 24 hours in comparison with control cells (Fig. 4d). RAD51 loading was enhanced after
188 MMS22L expression was restored. From these observations, we conclude that MMS22L loss
189 confers high sensitivity to PARPis due to compromised RAD51 recruitment to PARPi-induced
190 DSBs, causing homologous recombination deficiency (HRD).
191 Tumors with HRD have been found to display specific patterns of genomic alterations,
192 which can be quantified using a HRD score based on genome-wide measuring three patterns of
193 genomic instability (loss of heterozygosity, telomeric allelic imbalance, and large-scale state
194 transitions) [41]. A high HRD score (≥42) has been shown to be predictive of clinical benefit with

195 PARPi or platinum therapy in breast and ovarian cancer patients [42,43]. Using whole-genome
196 sequencing data, we previously showed that a subset of PCa patients with a high HRD score
197 did not harbor germline or somatic mutations in BRCA1/2 and other HRR genes [44]. Further
198 analysis revealed that tumors with MMS22L heterozygous or homozygous deletion displayed
199 significantly higher HRD scores (Fig. 4e), although much higher scores were observed in tumors
200 with homozygous deletion. Tumors with both BRCA and MMS22L deficiency had the highest
201 HRD score. The MMS22L loss-mediated genomic instability was further confirmed using
202 HRDetect (Supplementary Fig. 6), a model that quantitatively aggregates six HRD-associated
203 signatures [45]. These results may partially explain previously uncharacterized cause of HRD in
204 PCa. In addition, using publicly available PCa clinical data, we found MMS22L deletion is
205 correlated with decreased MMS22L transcript levels (Fig. 4f). Tumors with heterozygous or
206 homozygous deletion had significantly lower MMS22L mRNA levels compared to those with
207 wild-type MMS22L. Patients with lower MMS22L expression had a shorter survival (Fig. 4g),
208 suggesting tumor progression driven by HRD-mediated genomic instability.

209 **The response to PARP inhibition after MMS22L loss is p53-dependent**

210 Next, we asked why deletion of MMS22L did not increase PARPi response in PC-3 and
211 DU145 cells (Fig. 3a). CRISPR screens revealed that TP53 was one of the top resistance genes
212 in LNCaP, C4-2B, and 22Rv1 cells (Fig. 1i; Supplementary Table 4). This was validated by
213 deletion of TP53 in these cell lines (Fig. 5a). LNCaP and C4-2B cells possess wild-type TP53,
214 while 22Rv1 cells harbor a mono-allelic TP53 mutation and have a relatively low p53 protein
215 level (Supplementary Table 1 and Supplementary Fig. 7). In contrast, PC-3 cells have TP53
216 truncating mutations and do not express p53 (p53-null), and DU145 cells harbor dominant
217 negative TP53 mutations [46]. Notably, PCa cell lines with TP53 mutations are generally less
218 sensitive to olaparib compared to cell lines with wild-type TP53 (Supplementary Fig. 1).
219 Furthermore, RNA-sequencing (RNA-seq) analysis revealed 271 commonly upregulated genes
220 in LNCaP and C4-2B cells after olaparib treatment, in which the p53 pathway is significantly

221 enriched (Fig. 5b,c; Supplementary Table 6), supporting the role of p53 activation in modulating
222 response to PARP inhibition. We reasoned that TP53 status might impact PARPi response of
223 MMS22L-deleted cells. Using an RNA interference approach, we showed that knockdown of
224 MMS22L expression significantly increased PARPi sensitivity in TP53 wild-type C4-2B cells,
225 whereas TP53-KO cells remained insensitive (Fig. 5d). Using a Dox-inducible system, we
226 reintroduced the TP53 gene into p53-null PC-3 cells. Restoration of p53 expression re-
227 sensitized MMS22L-KO PC-3 cells to olaparib *in vitro* and *in vivo* (Fig. 5e, f). We observed that
228 the level of γ-H2AX protein expression and foci were increased after restoration of p53
229 expression in MMS22L-KO PC-3 cells, indicating more DNA DSBs (Fig. 5g,h). Accordingly, cell
230 apoptosis was increased as determined by cleaved PARP levels. These results suggest that
231 MMS22L deletion increases PARPi sensitivity only when p53 remains functional. While 6% of
232 primary and 15.5% of metastatic tumors contain concurrent genomic alterations of MMS22L and
233 TP53, approximately 27% of primary and 20.5% of metastatic prostate tumors harbor wild-type
234 TP53 and MMS22L deletion when heterozygous deletion is counted (Fig. 5i). To further identify
235 MMS22L deletion in clinical samples, we utilized DNAscope assay, a new chromogenic DNA *in*
236 *situ* hybridization technique, on a tissue microarray (TMA) with 146 primary PCa tissue cores.
237 We detected 4.1% homozygous deletion and 26% heterozygous deletion of MMS22L in primary
238 PCa patients (Fig. 5j; Supplementary Fig. 8). Together, our results suggest that loss of MMS22L
239 occurs in a considerable fraction of PCa patients, who may therefore benefit from PARP
240 inhibition.

241 **Validation of positively selected genes related to PARPi resistance**

242 Next, we set out to investigate PARPi resistance. We found that the top positively selected
243 genes include those previously identified as conferring PARPi resistance in other contexts,
244 including PARP1, PARP2, PARG, ADPRHL2 (also known as ARH3), and TP53BP1 (Fig. 1i) [3,47-
245 50]. Although not altered as frequently as TP53 in PCa, downregulation of these genes could
246 influence PARPi response. PPP2R2A was previously included in the HRR gene list used to

247 select patients for the PROfound trial (NCT02987543). However, the FDA subsequently
248 removed PPP2R2A from the approved HRR gene panel because outcomes appeared worse for
249 patients with PPP2R2A alterations with olaparib compared to the control [6]. In accordance with
250 the clinical result, we identified PPP2R2A as one of the common hits from positive selection
251 (Fig. 1i; Supplementary Table 4). PPP2R2A is located on chromosome 8p and frequently
252 deleted in PCa (Supplementary Fig. 9). Indeed, chromosome 8p is the most frequent lost
253 chromosomal arm of all tumors (36%) in the TCGA cohort [35,51,52], suggesting a potentially
254 common intrinsic resistance mechanism in tumors with 8p loss.

255 Surprisingly, we identified Checkpoint kinase 2 (CHEK2) as one of the top resistance genes
256 in LNCaP, C4-2B and 22Rv1 cells. This is an unexpected result since CHEK2 is one of the
257 previously reported BRCAness genes [53] and an FDA-approved biomarker for olaparib in the
258 treatment of mCRPC patients. CHEK2 has been used as a biomarker of PARPi sensitivity in
259 several PARPi clinical trials [7-10,54,55] because of its known function in promoting HRR through
260 phosphorylation of BRCA1 [56,57]. We deleted CHEK2 in five PCa cell lines and observed
261 significantly increased resistance in LNCaP, C4-2B, 22Rv1 cells, but not in TP53-mutant PC-3
262 and DU145 cells using cell viability and colony formation assays (Fig. 6a,b). We further
263 generated CHEK2-KO C4-2B single cell clones, which all displayed resistance to olaparib (Fig.
264 6c). The resistance was also observed with other PARPis (rucaparib, talazoparib and veliparib)
265 and carboplatin using C4-2B and 22Rv1 cell models (Fig. 6d). We conclude that CHEK2 loss is
266 associated with PARPi resistance rather than sensitivity in PCa with functional TP53.

267 **Loss of CHEK2/TP53 enhances HRR function through E2F7-controlled BRCA2**
268 **expression**

269 CHEK2 regulates multiple proteins beyond BRCA1 in response to DNA damage. CHEK2
270 phosphorylates p53 on serine 20 and stabilizes p53, leading to cell cycle arrest in G1 phase
271 [58,59]. We therefore asked whether PARPi resistance caused by CHEK2 loss is mediated through
272 p53 inactivation. In line with activation of p53 pathway after PARP inhibition (Fig. 5c), we found

273 that olaparib treatment increased phosphorylated CHEK2 and p53 protein expression levels in
274 CHEK2-intact C4-2B and 22Rv1 cells, but not in CHEK2-KO cells (Fig. 7a). The extent of DNA
275 DSBs was also greater in CHEK2-intact cells compared to CHEK2-KO cells following olaparib
276 treatment as measured by γ-H2AX protein expression and foci (Fig. 7a,b). Accordingly, there
277 was increased olaparib-induced apoptosis in CHEK2-intact cells as measured by cleaved-PARP
278 levels (Fig. 7a). Deletion of TP53 had no effect on olaparib-induced CHK2 phosphorylation but
279 reduced DNA DSBs (γ-H2AX foci) and cell apoptosis (cleaved-PARP) as similarly observed in
280 CHEK2-KO cells (Fig. 7c).

281 Next, we sought to investigate the CHEK2-TP53 downstream target genes that may
282 contribute to PARPi resistance in CHEK2-KO cells. Previous studies have shown that E2F7 is a
283 TP53-reulated gene [60], and that deletion of E2F7 renders cells resistant to PARP inhibition
284 through upregulation of RAD51 in BRCA2-deficient cells [61]. E2F7 was also one of the top
285 positively selected genes in our CRISPR screens (Fig. 1i). E2F7 is an atypical member of the
286 E2F transcription factor family, which regulates its target genes, including HRR genes, through
287 transcription repression rather than activation. We reasoned that CHEK2 loss might derepress
288 HRR gene expression via the TP53-E2F7 axis. To investigate TP53-mediated regulation of
289 E2F7 expression, we analyzed publicly available p53 ChIP-seq data in multiple cell lines and
290 found highly enriched p53 binding immediately upstream of the E2F7 transcription start site
291 (TSS) (Supplementary Fig. 10a), indicating a conserved and direct transcriptional regulation
292 mechanism. Using p53 ChIP-qPCR, we observed baseline p53 binding at the E2F7 promoter,
293 which was significantly increased after olaparib treatment in CHEK2-intact C4-2B and 22Rv1
294 cells (Fig. 7d). However, olaparib-induced p53 binding was not observed after CHEK2 loss.
295 Accordingly, E2F7 expression was increased after olaparib treatment in CHEK2-intact C4-2B
296 cells within a few hours, but not in CHEK2-KO cells (Fig. 7e). Furthermore, the MDM2 inhibitor
297 (MDM2i) nutlin, an agent that blocks MDM2-mediated ubiquitination and promotes p53
298 stabilization and activity, increased p53 expression and p53 binding at the E2F7 promoter as

299 well (Supplementary Fig. 10b,c), supporting p53-regulated E2F7 expression. Indeed, MDM2i
300 treatment overcame olaparib resistance as a result of CHEK2 deletion in line with the role of
301 TP53-E2F7 axis in PARPi resistance (Supplementary Fig. 10d).
302 To investigate E2F7-controlled HRR gene expression, we analyzed publicly available E2F7
303 ChIP-seq data in multiple cell lines and observed strong E2F7 binding immediately upstream of
304 the TSSs of BRCA1/2 and RAD51 genes (Supplementary Fig. 10e). Using E2F7 ChIP-qPCR,
305 we demonstrated strong E2F7 binding at these genomic regions in both CHEK2-intact and
306 CHEK2-KO C4-2B and 22Rv1 cells (Fig. 7f). Importantly, E2F7 binding was significantly
307 increased in CHEK2-intact control cells after olaparib treatment but remained unchanged or
308 significantly decreased in CHEK2-KO cells. In agreement with the E2F7 ChIP results, we found
309 that mRNA levels of BRCA1/2 and RAD51 were significantly decreased after olaparib treatment
310 in CHEK2-intact C4-2B cells but increased in CHEK2-KO cells (Fig. 7g), indicating E2F7-
311 mediated transcriptional suppression on HRR genes. It should be noted that no significant cell
312 cycle alterations were observed after CHEK2 or TP53 deletion in C4-2B cells (Supplementary
313 Fig. 11a). Therefore, upregulation of BRCA1/2 and RAD51 gene expression is largely due to
314 transcriptional regulation rather than cell cycle alteration, although the expression of HRR genes
315 is cell cycle-dependent. The protein levels of BRCA1/2 and RAD51 were decreased as well
316 after olaparib treatment in CHEK2-inatct cells (Fig. 7h). However, the protein expression
317 changes were not all consistent with the mRNA expression levels in CHEK2-KO cells. While the
318 BRCA2 and RAD51 protein levels were increased or remained at a high level following olaparib
319 treatment, the BRCA1 protein level was decreased. This is likely because BRCA1 is directly
320 regulated by CHEK2 through posttranslational modification [56]. On the other hand, the reduction
321 of BRCA1 protein expression was not observed in TP53-KO cells since p53 is a downstream
322 effector of CHEK2 (Supplementary Fig. 11b). These results suggest that the CHEK2-TP53-
323 E2F7 axis is activated after olaparib treatment, leading to suppression of HRR gene expression,
324 and that this axis is disrupted when either CHEK2 or TP53 is lost. Specifically, the protein level

325 of the BRCA2 gene was significantly upregulated after CHEK2 or TP53 loss. In addition, we
326 found that olaparib-induced BRCA2 suppression was rescued after knockdown of E2F7,
327 rendering cell resistant to olaparib (Fig. 7i; Supplementary Fig. 11c).
328 To determine whether HRR capacity was enhanced after CHEK2 loss, we performed
329 RAD51 foci formation assay and found significantly increased olaparib-induced RAD51 foci in
330 CHEK2-KO C4-2B and 22Rv1 cells (Fig. 7j). These results suggest that the PARPi resistance
331 arising from CHEK2 loss is, at least in part, dependent on enhanced HRR function. To further
332 determine whether increased BRCA2 expression is responsible for PARPi resistance after
333 CHEK2 loss, we knocked down BRCA2 in CHEK2-KO C4-2B and 22Rv1 cells and found that
334 these cells were re-sensitized to olaparib (Fig. 7k). Similarly, knockdown of BRCA2 in TP53-KO
335 cells increased olaparib sensitivity (Supplementary Fig. 11d). In agreement with these results,
336 we found that there was a negative correlation between CHEK2 and BRCA2 protein expression
337 in the TCGA cohort (Fig. 7l). Together, our results support the notion that the CHEK2-TP53-
338 E2F7-BRCA2 pathway is one of the primary resistance mechanisms for PARP inhibition after
339 CHEK2 loss (Fig. 7m).
340 **ATR inhibition overcomes PARPi resistance in CHEK2-deficient PCa cells.**
341 Finally, we sought to explore therapeutic strategies to overcome PARPi resistance after
342 CHEK2 loss. Emerging evidence has shown that PARPi resistance is often accompanied by
343 increased ATR activity, which coordinates cell cycle checkpoint response through
344 phosphorylation of CHK1 and allows cells to survive PARPi-induced replication stress [62]. We
345 found that ATR activity was elevated in CHEK2-KO cells after olaparib treatment, as evidenced
346 by increased CHK1 phosphorylation in a dose-dependent manner (Supplementary Fig. 12). We
347 treated CHEK2-KO cells with olaparib in combination with M6620, a clinically used ATR inhibitor
348 (ATRi) [63]. M6620 was remarkably more effective when combined with olaparib in cell viability
349 assays (Fig. 8a). The combination therapy profoundly suppressed cell colony formation of
350 CHEK2-KO cells in a synergistic manner, as demonstrated by the HSA and Bliss synergy

351 scores [64,65] (Fig. 8b). Using *in vivo* xenograft models, we observed that CHEK2-KO C4-2B and
352 22Rv1 tumors did not respond to olaparib or M6620 as a single agent. However, the
353 combination treatment abolished the tumor growth (Fig. 8c and Supplementary 13). We did not
354 observe any weight loss in each group, indicating the combination therapy was well-tolerated.
355 Mechanistically, M6620 inhibited CHK1 phosphorylation as expected (Fig. 8d). The combination
356 treatment significantly inhibited BRCA1/2 and RAD51 expression in CHEK2-KO C4-2B and
357 22Rv1 cells, leading to more DNA damage and cell apoptosis as determined by γ-H2AX and
358 cleaved-PARP expression. Functionally, olaparib-induced RAD51 formation was completely
359 abolished in CHEK2-KO cells when they were treated with M6620 in combination with olaparib
360 (Fig. 8e).

361 **DISCUSSION**

362 In this study, we provided a systematic view of the genetic determinants and mechanisms
363 underlying the sensitivity and resistance of PCa to PARP inhibition beyond BRCA1/2 alterations.
364 We identified genes, such as RAD51B, RAD54L, FANCL, that have already been used as
365 biomarkers for PARP inhibition in the FDA-approved genetic test for mCRPC patients, as well
366 as previously unknown genes. These new genes could serve as predictive biomarkers for PARP
367 inhibition if mutated or deleted in PCa or therapeutic targets through pharmacologic inhibition in
368 combination with PARPis. One such novel hit is MMS22L, a gene located in a genomic region
369 frequently deleted in PCa, loss of which significantly increases the response to PARPis.
370 Mechanistically, MMS22L forms a complex with TONSL, which accumulates at distressed
371 replication forks and is required for the HRR of replication fork-associated DSBs through
372 promoting RAD51 loading [38,39,66]. When MMS22L is deleted, cells fail to load RAD51 to PARPi-
373 induced collapsed replication forks, leading to accumulation of DSBs, cell cycle arrest at G2/M
374 phase, and apoptotic cell death. The HRR function of MMS22L-TONSL seems specific to the
375 recovery of collapsed replication forks and does not act through BRCA2 [38]. Interestingly,
376 MMS22L deletions appear to be an early event in prostate tumorigenesis since they are more

377 frequently detected in primary tumors. If the use of PARPis in localized PCa (e.g., in the
378 neoadjuvant/adjuvant setting) is found to confer clinical benefit as has been suggested in breast
379 cancer with BRCA mutations [67], detection of MMS22L deletion would identify a much larger
380 population of patients who may benefit. In addition, our data suggest that cells with partial loss
381 of MMS22L (i.e., monoallelic loss) are equally sensitive to PARP inhibition compared to
382 complete loss (i.e., biallelic loss) likely due to insufficient MMS22L-TONSL complex formation.
383 This is further supported by the evidence from clinical sample analyses, showing significantly
384 lower mRNA levels and higher HRD scores in both homozygous and heterozygous MMS22L
385 deletion tumors. Identification of MMS22L as a new BRCAness gene explains a significant part
386 of patients that have high HRD scores but without HRR gene alterations per the olaparib label.
387 Given a considerable number of PCa patients with MMS22L deletion detected by next
388 generation sequencing- or DNA *in situ* hybridization-based assays, this genomic alteration may
389 be a valuable biomarker for PARP inhibition despite the fact that the response is p53-
390 dependent.

391 Previous studies of PARPi resistance have been focusing on acquired resistance
392 mechanisms in BRCA1/2-deficient cancers, showing that residual or restored HRR activity is the
393 most commonly observed resistance mechanism. This can be achieved by secondary or
394 reversion mutations of BRCA1, BRCA2 and RAD51 isoforms [68-70], loss of BRCA1 promoter
395 methylation [71], increased expression of hypomorphic isoforms of BRCA1 [72,73], loss of TP53BP1
396 and resection-associated factors RIF1, REV7, and Shieldin [49,74-76]. In contrast, our work
397 uncovers an intrinsic resistance mechanism in BRCA1/2-sufficient PCa cells, involving two
398 frequently mutated tumor suppressor genes TP53 and CHEK2. The role of TP53 and its
399 upstream activator CHEK2 in a set of tightly regulated cell cycle checkpoints and DDR events
400 has been extensively studied. In response to DNA DSBs, cells activate CHEK2 that
401 phosphorylates and stabilizes p53, leading to cell cycle arrest to allow for DNA repair or
402 inducing apoptosis after genotoxic damage. However, the PARPi resistance caused by loss of

403 CHEK2 or TP53 cannot be fully explained by impaired p53-mediated apoptosis. Indeed, PARPi
404 can trigger apoptotic cell death in TP53-deficient PCa cells [77]. High-grade serous ovarian cancer
405 (HGSOC) patients with defects in HRR are highly sensitive to PARP inhibition despite the fact
406 that TP53 mutations are detected in 96% HGSOC tumors [78]. Here, we propose an as yet
407 uncharacterized pathway that underlies the resistance of PCa cells to PARP inhibition. We show
408 that PARP inhibition activates the CHEK2-TP53-E2F7 pathway that suppresses the expression
409 of HRR genes and potentiates the cytotoxicity of PARPis. Loss of CHEK2 or TP53, however,
410 markedly reduces the expression of their downstream target E2F7, leading to increased HRR
411 gene (largely BRCA2) expression due to lack of E2F7-mediated transcriptional suppression.
412 Upregulation of BRCA2 enhances HRR capacity sufficient for the repair of PARPi-induced
413 DSBs and cell survival. Interestingly, BRCA1 is another direct target of the CHEK2 kinase. The
414 fact that loss of CHEK2 leads to PARPi resistance instead of sensitivity is unexpected. We show
415 that loss of CHEK2 may compromise BRCA1 regulation; after all, the BRCA1 protein expression
416 is not completely abolished. On the other hand, the CHEK2-TP53-E2F7 pathway has
417 predominantly emerged after PARP inhibition. Our finding is consistent with the results from
418 recent clinical trials which show little benefit in patients with mutations in CHEK2 [8,10,79], providing
419 a rationale to revisit FDA-approved clinically-used biomarkers for the use of olaparib. Our data
420 support the notion that HRR deficiency resulting from alterations in non-BRCA genes is unlikely
421 to be of similar therapeutic relevance in comparison to BRCA2 deficiency, considering that
422 mutations in the TP53 gene occur in more than 50% of all cancers. Conversely, PCa harboring
423 BRCA2 deficiency more likely respond to PARP inhibition regardless of TP53 status. This is
424 consistent with our CRISPR screen results, showing that BRCA2 was identified as one of the
425 top hits in TP53-mutated DU145 cells, while many of the canonical HRR genes (including
426 Fanconi anemia genes) were not negatively selected. Further investigation is needed to
427 determine which genomic alterations in the HRR pathway can or cannot be rescued by
428 upregulation of BRCA2 after loss of CHEK2 or TP53. We recently reported that RB1, another

429 frequently mutated tumor suppressor gene, may also confer resistance to PARP inhibition
430 through E2F1-mediated upregulation of HRR genes [36], indicating the importance and complexity
431 of E2F transcriptional network through activation and repression in the context of DNA repair.
432 The finding of the TP53/E2F7- and RB1/E2F1-mediated resistance mechanisms is clinically
433 relevant since TP53 and RB1 are concurrently altered in 39% of mCRPC tumors with
434 adenocarcinoma histology and 74% of mCRPC tumors with neuroendocrine features [80,81].
435 Current clinical use of PARPis is guided by mutations of a single gene and overlooks common
436 concurrent genomic alterations that may have an antagonistic effect.
437 Finally, we propose a therapeutic approach with combined PARP and ATR inhibition to
438 overcome PARPi resistance. Mechanistically, in order to survive PARP inhibition, cancer cells
439 rely more on ATR checkpoint to slow down cell cycle and reduce replication stress for repairing
440 DSBs. ATR inhibition increases replication origin firing and DNA synthesis despite the presence
441 of PARPi-induced replication fork gaps, leading to progressive accumulation of DSBs [20].
442 Moreover, ATR inhibition can disrupt RAD51 loading to stalled replication forks and DSBs in
443 PARPi-resistant BRCA1-deficient cells [82]. Our results further demonstrate that blocking ATR
444 activity inhibits HRR gene expression and RAD51 foci formation, leading to a high number of
445 stalled replication forks collapsing into toxic, irreparable DSBs. Indeed, the combination of
446 PARPi with ATRi was synergistic in many PARPi-resistant models regardless of their resistance
447 mechanisms [62]. Simultaneous suppression of ATR and PARP may be a preferred strategy to
448 overcome PARPi resistance.
449
450

451 **METHODS**

452 **Cell Lines and Materials**

453 Prostate cancer cell lines LNCaP, C4-2B, 22Rv1, PC-3, DU145, and MDA PCa 2b were
454 obtained from American Type Culture collection (ATCC). Cells were cultured following the
455 provider's recommendations. The identity of the cell lines was confirmed based on high-
456 resolution small tandem repeats (STR) profiling at Dana-Farber Cancer Institute (DFCI)
457 Molecular Diagnostics Core Laboratory and exome-sequencing analyses performed by LC
458 Sciences. Cells were regularly tested for mycoplasma. All reagents (including antibodies, small
459 molecule inhibitors, oligonucleotides, and plasmids) used in this study are listed in
460 Supplementary Table 7.

461 **Cellular Viability Assay**

462 PCa cells were seeded in 96-well plates with 1000-3000 cells/well (n = 6) and treated as
463 indicated. Cellular viability assays were performed using alamarBlue (ThermoFisher Scientific)
464 5-10 days after treatments and repeated 2–3 times.

465 **Clonogenic Assay**

466 PCa cells were seeded in 12-well plates at low density to avoid contact between clones.
467 Subsequently, cells were treated as indicated and allowed to grow for 10-14 days. Colonies
468 were fixed with paraformaldehyde (4%) for 20 minutes and stained with crystal violet (0.1%) for
469 15 minutes. Colony images were quantified using ImageJ software (National Institutes of
470 Health).

471 **Cell Growth Competition Assay**

472 MMS22L-KO and AAVS1 control cells were infected with lentiviruses generated using LV-GFP
473 (Addgene #25999) or LV-RFP (Addgene #26001) plasmid, respectively. MMS22L-KO LNCaP
474 and C4-2B cells stably express GFP, whereas control cells stably express RFP. GFP or RFP
475 positive cells were collected by the BD FACSAria cell sorter (BD Biosciences) and mixed in a

476 1:1 ratio. The mixed cell populations were incubated for 7 days with 3 uM of olaparib or DMSO
477 treatment, followed by collection and calculation of GFP and RFP positive cells.

478 **Drug Synergy analysis**

479 Cells were seeded in 12-well plates and treated with vehicle and 4 doses of olaparib (200, 300,
480 500 and 1000 nM) and M6620 (20, 30, 50 and 100 nM) in a matrix format to include 25 different
481 dose combinations. Colonies were quantified on day 14 using imageJ. Drug synergy scores
482 were calculated based on the HSA and Bliss model using the SynergyFinder2.0 [64].

483 **RNA Interference**

484 E2F7 and BRCA2 siRNAs and negative control siRNA were purchased from Sigma-Aldrich.
485 Cells were seeded onto 6-well or 96-well plates for 24 hours and followed by siRNA (10 nM)
486 transfection using Lipofectamine RNAiMAX (Invitrogen) according to the manufacturer's
487 protocol. The siRNA sequences are listed in Supplementary Table 7.

488 **Cell Cycle Analysis**

489 Cells were plated in 6-cm dishes with or without olaparib treatment for 72 hours. Collected cells
490 were labelled using Click-iT® EdU Flow Cytometry Assay Kit (Invitrogen) according to the
491 manufacturer's protocol and followed by flow cytometry using BD LSR Fortessa (BD
492 Biosciences).

493 **Chromatin Immunoprecipitation Quantitative PCR (ChIP-qPCR)**

494 ChIP experiments were performed as previously described [83,84]. Briefly, PCa cells were grown in
495 regular media and treated with olaparib (10 μM) for 24 hours prior to ChIP. Cells were cross-
496 linked by formaldehyde (1%) at room temperature (RT) for 10 minutes. After washing with ice-
497 cold PBS, cells were collected and lysed. The soluble chromatin was purified and fragmented by
498 sonication. Immunoprecipitation (IP) was performed using normal IgG or p53 or E2F7 antibody
499 (2 μg/IP). ChIP DNA was extracted and analyzed by qPCR using iTaq Universal SYBR Green
500 Supermix (Bio-Rad). The primer sequences are listed in Supplementary Table 7.

501 **Quantitative RT-PCR (RT-qPCR)**

502 Total RNA was extracted using RNeasy Mini Kit (Qiagen) according to the manufacturer's
503 protocol. RT-qPCR was performed as previously described [85]. The primer sequences are listed
504 in Supplementary Table 7.

505 **RNA Sequencing (RNA-seq)**

506 LNCaP and C4-2B cells were treated with olaparib (3 μM) or DMSO in biological duplicates.
507 Total RNAs were extracted using RNeasy Mini Kit (Qiagen). RNA-Seq library preparation and
508 next generation sequencing by Illumina HiSeq were conducted using GENEWIZ services.

509 ***In vivo* Xenograft studies**

510 All mice were maintained in compliance with the guidelines approved by the Institutional Animal
511 Care and Use Committee (IACUC) at the Brigham and Women's Hospital. For xenograft
512 studies, male ICR/SCID mice and male NCG mice (NOD-*Prkdc*^{em26Cd52}*Il2rg*^{em26Cd22}/NjuCrl) at 4-5
513 weeks of age were purchased from Tconic Bioscience and Charles River Laboratories,
514 respectively. For the PC-3 xenograft assay, 2.5 million cells were prepared in 50 µl PBS and
515 mixed with 50 µl Matrigel (Corning Matrigel Matrix High Concentration #354262) to form a total
516 of 100 µl cell suspension and followed by the subcutaneous inoculation in male ICR/SCID mice.
517 Tumor volume was calculated using the modified ellipsoid formula: length x width^2/2. After
518 tumors developed to a volume of approximately150 mm^3, mice were randomized into 4 groups
519 (vehicle: n = 9, doxycycline: n = 5, olaparib: n = 5, and doxycycline plus olaparib: n = 5). Mice
520 were treated with vehicle (5% DMSO/10% d-a-tocopherol polyethylene glycol 1000 succinate;
521 oral gavage, OG), doxycycline (10 mg/kg in 10% d-a-tocopherol polyethylene glycol 1000
522 succinate; intraperitoneal, IP), olaparib (50 mg/kg in 5%DMSO/10% d-a-tocopherol polyethylene
523 glycol 1000 succinate; OG) or doxycycline (IP) plus olaparib (OG). Treatment was administered
524 every day for doxycycline and 5 days a week for vehicle and olaparib.
525 For the C4-2B and 22Rv1 xenograft assays, 5 million cells of C4-2B or 2.5 million cells of 22Rv1
526 were prepared as above. After tumors developed to a volume of approximately150 mm^3, mice

527 were randomized into 4 groups (vehicle, olaparib, M6620, and combination treatment) with 4
528 mice in each group. Mice were treated with vehicle, olaparib, M6620 (25 mg/kg in
529 5%DMSO/10% d-a-tocopherol polyethylene glycol 1000 succinate) or combination treatment
530 (olaparib 50 mg/kg and M6620 25 mg/kg in 5%DMSO/10% d-a-tocopherol polyethylene glycol
531 1000 succinate) through OG. Treatment was administered 5 days a week for single agent, and
532 5 days a week of olaparib plus 4 days a week of M6620 for combination treatment. Tumor
533 volume was manually measured every 3 days.

534 **Immunoblot analysis**

535 Cells were lysed in RIPA buffer supplemented with Halt™ protease and phosphatase inhibitor
536 cocktail (ThermoFisher Scientific). The protein concentration was determined using Pierce BCA
537 Protein Assay Kit (ThermoFisher Scientific). Proteins were resolved in SDS-polyacrylamide gels
538 (4–12%) and transferred to PVDF membranes using a Tris-glycine buffer system. Membranes
539 were blocked with 5% non-fat milk in 0.1% Tween20 in TBS (TBS-T) for 1 hour at room
540 temperature followed by incubation with primary antibodies and subsequently corresponding
541 secondary antibodies in 5% milk TBS-T. The membranes were developed with Immobilon
542 substrate (EMD Millipore).

543 **PAR immunoblotting**

544 The assay was performed according to the protocol as previously described [48]. Briefly, cells
545 were grown on 10 cm dishes for 24 hours to achieve 90% confluency. Cells were treated with
546 olaparib and/or PDDX-001 in the presence or absence of 0.01% MMS for a short period of time
547 as indicated. For total protein extraction, cells were lysed in RIPA buffer supplemented with
548 protease and phosphatase inhibitor cocktail and 1 μM PARG inhibitor ADP-HPD (Merck). For
549 chromatin fraction, cells were lysed and each fraction was collected using Subcellular Protein
550 Fractionation Kit (ThermoFisher Scientific) according to the manufacturer's protocol.
551 Immunoblotting was carried out as described in above.

552 **Immunofluorescence Analyses**

553 Cells were grown in a poly-L lysine-coated 4 well Millicell EZ slides (EMD Millipore) for 48 hours
554 and pre-extracted with 0.2% Triton-X on ice 90 seconds before fixation with 4%
555 paraformaldehyde in PBS for 20 minutes at room temperature (RT) and then permeabilized by
556 incubation with ice-cold methanol. After permeabilization, cells were blocked with 5% BSA in
557 PBS for 1 hour at RT, followed by incubation with 5% BSA in TBS-T containing primary
558 antibodies at a ratio of 1:200 overnight at 4°C. Cells were washed and incubated with secondary
559 fluorescent antibodies for 1 hour at RT. Alexa Fluor 488 anti-rabbit and Alexa Fluor 488 anti–
560 mouse antibodies were purchased from Invitrogen. After washing, the nuclear content was
561 stained with Mounting Medium with DAPI (Abcam) overnight at 4°C. Images were obtained with
562 fluorescence microscope BX53 (Olympus). Images were quantitatively assessed using ImageJ
563 software (NIH, Bethesda, MD) with 'Find maxima' function. More than 100 cells were analyzed
564 per condition in each experiment in a blinded manner.

565 **Generating Knockout Cell Lines Using CRISPR/Cas9 Gene Editing**

566 CRISPR guides targeting each gene were cloned into lentiGuide-Puro vector (#52963;
567 Addgene). The sgRNA sequences are listed in the Supplementary Table 7. The lentiCas9-Blast
568 vector that expresses Cas9 was obtained from Addgene (#52962). Lentiviruses were generated
569 using packaging vectors pMD2.G (#12259; Addgene) and psPAX2 (#12260; Addgene) with
570 Lipofectamine™3000 transfection reagents (#L3000015; Invitrogen) in 293FT cells. PCa cells
571 were infected with lentiviruses expressing Cas9 and selected with Blasticidin (10 μg/ml) to
572 establish stable Cas9-expressing cell lines. Polybrene was added at a final concentration of
573 8ug/ml to increase infecting efficiency. To generate KO cells, PCa cells were infected with
574 lentiviruses containing specific sgRNA and selected with puromycin (3 μg/ml). KO efficacy was
575 determined by immunoblot analyses. Single cell clones of MMS22L-KO and CHEK2-KO were
576 generated using BD FACSAria cell sorter (BD Biosciences) and followed by expansion.

577 **Generation of TET-inducible Exogenous MMS22L- or P53-expressing Cells**

578 MMS22L-KO and control C4-2B clone cells were infected with viruses containing TET-inducible
579 MMS22L gene. The MMS22L cDNA was created to be resistant to MMS22L sgRNA1 by the
580 introduction of silent mutations in the crispr RNA (crRNA) recognition sequence (change
581 CTTGGCAGGAATATAGCACAA to **CTAGGTAGA**AATATAGCACAA).
582 After neomycin (500 mg/ml) selection, doxycycline (0.15 μg/ml) treatment induces the MMS22L
583 expression confirmed by immunoblot. In addition, MMS22L-KO PC-3 cells were infected with
584 viruses containing TET-inducible WT TP53. Neomycin selection and the confirmation of p53
585 expression were performed as above. The MMS22L and TP53 cDNAs were cloned into the
586 Lenti-TRE3G-ORF-IRES-tRFP-PGK-Tet3G-neo vector, respectively. The plasmids were
587 custom-designed and synthesized at Transomic Technologies, Inc.
588 **Genome-wide CRISPR-Cas9 Knockout Screen**
589 We used genome-wide CRISPR-Cas9 KO H1 and H2 libraries obtained from Drs. Myles Brown
590 and X. Shirley Liu's laboratories [15], consisting of over 180,000 sgRNAs (10sgRNAs per gene).
591 For the CRISPR-Cas9 KO screens, 200 million PCa cells were infected with the lentiviral
592 CRISPR-Cas9 KO H1 and H2 libraries at a low multiplicity of infection (~0.3) to to maximize the
593 number of cells that have only one sgRNA integration. After 5 days of puromycin selection, the
594 surviving cells were expanded. Following preparation of 60 million cells for each condition to
595 achieve a representation of at least 300 cells per sgRNA, cells were divided into day 0 control
596 cells and cells cultured for 28 days (nine passages) treated with DMSO or olaparib before
597 genomic DNA extraction and library preparation. We used olaparib at the concentration of 5 μM
598 for LNCaP and C4-2B cells and 10 μM for 22Rv1 and DU145 cells. These concentrations were
599 close to the half maximal inhibitory concentration (IC50) for each cell line and allowed us to
600 identify both negatively (depleted) and positively (enriched) selected sgRNAs corresponding to
601 gene knockouts that increase and decrease olaparib response respectively. PCR was
602 performed using genomic DNA to construct the sequencing libraries. Each library was

603 sequenced at 30-40 million reads to achieve ~300 x average coverage over the CRISPR library.
604 The library from day 0 sample of each screen served as controls to identify positively or
605 negatively selected genes.

606 **CRISPR-Cas9 KO Screen Data Analysis**

607 CRISPR-Cas9 KO screen data was analyzed using the MAGeCK and MAGeCK-VISPR
608 algorithms [86,87]. MAGeCK calculated the read counts for each sgRNA. MAGeCK-VISPR
609 calculated the β-score for each gene by using AAVS1 gene as control. Comparison of the
610 differential β-score between olaparib treatment and DMSO treatment was performed using
611 MAGeCKFlute [17,18]. We ranked genes by differential β-score and robustly estimated σ, which is
612 the standard deviation of the differential β-score by a "quantile matching" approach. A cut-off
613 value was set to correspond 99 % of the data falling within 2σ, which defined genes with lower
614 β-scores than minus σ and higher β-scores than σ as negatively and positively selected genes,
615 respectively. Identified genes were further analyzed using STRING protein interaction analysis
616 [21]. GO analysis was performed using DAVID bioinformatics resources (https://david.ncifcrf.gov).

617 **DNAscope Assay Using Tissue Microarray (TMA)**

618 The TMA was constructed using primary prostate tumors retrieved from the Vancouver Prostate
619 Centre Tissue Bank as previously reported as approved by the institutional Review Board [88]. A
620 total of 146 tissue cores from 73 patients who had undergone radical prostatectomy were
621 included in this study. The DNAscope assay (Advanced Cell Diagnostics, Newark, CA) is a
622 chromogenic DNA in situ hybridization assay using two sets of target specific probes. Two
623 custom-designed probes were synthesized by Advanced Cell Diagnostics. DS-Hs-MMS22L-C1
624 is the probe targeting 29194-49180 of hg38 DNA range = chr 6:97142161-97283437. DS-Hs-
625 CEP6p-C2 is the control probe targeting 20891-35730 of hd38 DNA range = chr 6: 57224489-
626 57312704. The assay was performed on the TMA using DNAscope™ HD Duplex Reagent Kit
627 (Advanced Cell Diagnostics) according to the manufacturer's protocol. Briefly, the tissue section

628 was pretreated to allow access to target DNAs and followed by hybridization with two sets of
629 probes. Two independent signal amplification systems were used to detect both target DNAs.
630 Probes were hybridized to a cascade of signal amplification molecules, culminating in binding of
631 enzyme-labeled probes. Two chromogenic substrates were used and probe targeted regions
632 were visualized in red for the MMS22L locus and blue for the control region (i.e., the
633 centromeric region of chromosome 6p). An increase in the number of red dots relative to blue
634 dots indicates a copy number gain or amplification, while a decrease in the number of red dots
635 or no red dots indicates a copy number loss or deletion. The images were evaluated and scored
636 both digitally by the software (Aperio ImageScope, Leica Biosystems) and visually by a
637 pathologist (L. Fazli, Vancouver Prostate Centre). The MMS22L wild-type was defined as the
638 ratio of the total number of red dots divided by the total number of blue dots (red/blue) greater
639 than 0.5. The heterozygous deletion was defined as the ratio of red/blue is between 0.1-0.5,
640 while the homozygous deletion was defined as the ratio of red/blue is below 0.1.

641 **RNA Sequencing Analysis**

642 Raw RNA-seq reads are aligned to the human genome version hg38 by using STAR aligner [89].
643 Gene counts are quantified by using HT-seq [90] with REFSEQ annotation. Differentially
644 expressed genes are identified by using DESeq2 [91] with cutoff of FDR < 0.01, and ranked by the
645 statistics. The GSEA software was used for determining the KEGG pathways [92].

646 **HRD and HRDetect Scores**

647 HRD and HRdetect scores were determined as previously described [44]. A total of 267 PCa
648 cases with whole genome sequencing data were analyzed using the scarHRD R package and
649 HRDetect algorithm [45,93].

650 **Statistical Analysis**

651 Statistical analyses were performed using the unpaired 2-tailed Student's *t* test or 2-way
652 ANOVA with a post hoc Tukey's honest significant difference (HSD) test when comparing at

653 least three conditions using the Prism software (GraphPad). *P*-values of less than 0.05 were
654 considered as statistically significant.

655 **Public Data Analysis**

656 Clinical data sets were analyzed using the cBio Portal for Cancer Genomics (cBioPortal;
657 www.cbioportal.org) and PCaDB [94] (http://bioinfo.jialab-ucr.org/PCaDB/). Integrated Genome
658 Viewer (https://www.broadinstitute.org/igv/) was used for visualization of ChIP-seq data
659 analysis. ChIP-seq data were obtained from ChIP-Atlas [95] (http://chip-atlas.org).

660

661 **Data Availability**

662 RNA-seq data are available under GEO accession number GSE189186.

663

664

665

666 **References**

667 1 Robinson, D. *et al.* Integrative Clinical Genomics of Advanced Prostate Cancer. *Cell* **162**,
668 454, doi:10.1016/j.cell.2015.06.053 (2015).
669 2 Armenia, J. *et al.* The long tail of oncogenic drivers in prostate cancer. *Nat Genet* **50**,
670 645-651, doi:10.1038/s41588-018-0078-z (2018).
671 3 Murai, J. *et al.* Trapping of PARP1 and PARP2 by Clinical PARP Inhibitors. *Cancer Res*
672 **72**, 5588-5599, doi:10.1158/0008-5472.CAN-12-2753 (2012).
673 4 Farmer, H. *et al.* Targeting the DNA repair defect in BRCA mutant cells as a therapeutic
674 strategy. *Nature* **434**, 917-921, doi:10.1038/nature03445 (2005).
675 5 Bryant, H. E. *et al.* Specific killing of BRCA2-deficient tumours with inhibitors of
676 poly(ADP-ribose) polymerase. *Nature* **434**, 913-917, doi:10.1038/nature03443 (2005).
677 6 Hussain, M. *et al.* Survival with Olaparib in Metastatic Castration-Resistant Prostate
678 Cancer. *N Engl J Med* **383**, 2345-2357, doi:10.1056/NEJMoa2022485 (2020).
679 7 de Bono, J. *et al.* Olaparib for Metastatic Castration-Resistant Prostate Cancer. *N Engl J*
680 *Med* **382**, 2091-2102, doi:10.1056/NEJMoa1911440 (2020).
681 8 de Bono, J. S. *et al.* Talazoparib monotherapy in metastatic castration-resistant prostate
682 cancer with DNA repair alterations (TALAPRO-1): an open-label, phase 2 trial. *Lancet*
683 *Oncol* **22**, 1250-1264, doi:10.1016/S1470-2045(21)00376-4 (2021).
684 9 Abida, W. *et al.* Rucaparib in Men With Metastatic Castration-Resistant Prostate Cancer
685 Harboring a BRCA1 or BRCA2 Gene Alteration. *J Clin Oncol* **38**, 3763-3772,
686 doi:10.1200/JCO.20.01035 (2020).
687 10 Abida, W. *et al.* Non-BRCA DNA Damage Repair Gene Alterations and Response to the
688 PARP Inhibitor Rucaparib in Metastatic Castration-Resistant Prostate Cancer: Analysis
689 From the Phase II TRITON2 Study. *Clin Cancer Res* **26**, 2487-2496, doi:10.1158/1078-
690 0432.CCR-20-0394 (2020).
691 11 Mateo, J. *et al.* Olaparib in patients with metastatic castration-resistant prostate cancer
692 with DNA repair gene aberrations (TOPARP-B): a multicentre, open-label, randomised,
693 phase 2 trial. *Lancet Oncol* **21**, 162-174, doi:10.1016/S1470-2045(19)30684-9 (2020).
694 12 Olivieri, M. *et al.* A Genetic Map of the Response to DNA Damage in Human Cells. *Cell*
695 **182**, 481-496 e421, doi:10.1016/j.cell.2020.05.040 (2020).
696 13 Zimmermann, M. *et al.* CRISPR screens identify genomic ribonucleotides as a source of
697 PARP-trapping lesions. *Nature* **559**, 285-289, doi:10.1038/s41586-018-0291-z (2018).
698 14 Clements, K. E. *et al.* Identification of regulators of poly-ADP-ribose polymerase inhibitor
699 response through complementary CRISPR knockout and activation screens. *Nat*
700 *Commun* **11**, 6118, doi:10.1038/s41467-020-19961-w (2020).
701 15 Jeselsohn, R. *et al.* Allele-Specific Chromatin Recruitment and Therapeutic
702 Vulnerabilities of ESR1 Activating Mutations. *Cancer Cell* **33**, 173-186 e175,
703 doi:10.1016/j.ccell.2018.01.004 (2018).
704 16 Xu, H. *et al.* Sequence determinants of improved CRISPR sgRNA design. *Genome Res*
705 **25**, 1147-1157, doi:10.1101/gr.191452.115 (2015).
706 17 Wang, B. *et al.* Integrative analysis of pooled CRISPR genetic screens using
707 MAGeCKFlute. *Nat Protoc* **14**, 756-780, doi:10.1038/s41596-018-0113-7 (2019).
708 18 Li, Z. *et al.* CRISPR Screens Identify Essential Cell Growth Mediators in BRAF Inhibitor-
709 resistant Melanoma. *Genomics Proteomics Bioinformatics* **18**, 26-40,
710 doi:10.1016/j.gpb.2020.02.002 (2020).
711 19 Gupte, R., Liu, Z. & Kraus, W. L. PARPs and ADP-ribosylation: recent advances linking
712 molecular functions to biological outcomes. *Genes Dev* **31**, 101-126,
713 doi:10.1101/gad.291518.116 (2017).

20 Simoneau, A., Xiong, R. & Zou, L. The trans cell cycle effects of PARP inhibitors underlie their selectivity toward BRCA1/2-deficient cells. *Genes Dev* **35**, 1271-1289, doi:10.1101/gad.348479.121 (2021).
21 Szklarczyk, D. *et al.* The STRING database in 2021: customizable protein-protein networks, and functional characterization of user-uploaded gene/measurement sets. *Nucleic Acids Res* **49**, D605-D612, doi:10.1093/nar/gkaa1074 (2021).
22 Hakem, R., de la Pompa, J. L., Elia, A., Potter, J. & Mak, T. W. Partial rescue of Brca1 (5-6) early embryonic lethality by p53 or p21 null mutation. *Nat Genet* **16**, 298-302, doi:10.1038/ng0797-298 (1997).
23 Ludwig, T., Chapman, D. L., Papaioannou, V. E. & Efstratiadis, A. Targeted mutations of breast cancer susceptibility gene homologs in mice: lethal phenotypes of Brca1, Brca2, Brca1/Brca2, Brca1/p53, and Brca2/p53 nullizygous embryos. *Genes Dev* **11**, 1226-1241, doi:10.1101/gad.11.10.1226 (1997).
24 Adam, S. *et al.* The CIP2A–TOPBP1 axis safeguards chromosome stability and is a synthetic lethal target for BRCA-mutated cancer. *Nat. Cancer* **2**, 1357-1371, doi:https://doi.org/10.1038/s43018-021-00266-w (2021).
25 Kollarovic, G., Topping, C. E., Shaw, E. P. & Chambers, A. L. The human HELLS chromatin remodelling protein promotes end resection to facilitate homologous recombination and contributes to DSB repair within heterochromatin. *Nucleic Acids Res* **48**, 1872-1885, doi:10.1093/nar/gkz1146 (2020).
26 Spruijt, C. G. *et al.* Dynamic readers for 5-(hydroxy)methylcytosine and its oxidized derivatives. *Cell* **152**, 1146-1159, doi:10.1016/j.cell.2013.02.004 (2013).
27 Gilmore, J. M. *et al.* WDR76 Co-Localizes with Heterochromatin Related Proteins and Rapidly Responds to DNA Damage. *PLoS One* **11**, e0155492, doi:10.1371/journal.pone.0155492 (2016).
28 Dayebgadoh, G., Sardiu, M. E., Florens, L. & Washburn, M. P. Biochemical Reduction of the Topology of the Diverse WDR76 Protein Interactome. *J Proteome Res* **18**, 3479-3491, doi:10.1021/acs.jproteome.9b00373 (2019).
29 Kluth, M. *et al.* 13q deletion is linked to an adverse phenotype and poor prognosis in prostate cancer. *Genes Chromosomes Cancer* **57**, 504-512, doi:10.1002/gcc.22645 (2018).
30 Brookman-Amissah, N. *et al.* Allelic imbalance at 13q14.2 approximately q14.3 in localized prostate cancer is associated with early biochemical relapse. *Cancer Genet Cytogenet* **179**, 118-126, doi:10.1016/j.cancergencyto.2007.08.017 (2007).
31 Dong, J. T., Chen, C., Stultz, B. G., Isaacs, J. T. & Frierson, H. F., Jr. Deletion at 13q21 is associated with aggressive prostate cancers. *Cancer Res* **60**, 3880-3883 (2000).
32 Lu, T. & Hano, H. Deletion at chromosome arms 6q16-22 and 10q22.3-23.1 associated with initiation of prostate cancer. *Prostate Cancer Prostatic Dis* **11**, 357-361, doi:10.1038/pcan.2008.4 (2008).
33 Hyytinen, E. R. *et al.* Defining the region(s) of deletion at 6q16-q22 in human prostate cancer. *Genes Chromosomes Cancer* **34**, 306-312, doi:10.1002/gcc.10065 (2002).
34 Kluth, M. *et al.* Deletion lengthening at chromosomes 6q and 16q targets multiple tumor suppressor genes and is associated with an increasingly poor prognosis in prostate cancer. *Oncotarget* **8**, 108923-108935, doi:10.18632/oncotarget.22408 (2017).
35 Stopsack, K. H. *et al.* Aneuploidy drives lethal progression in prostate cancer. *Proc Natl Acad Sci U S A* **116**, 11390-11395, doi:10.1073/pnas.1902645116 (2019).
36 Miao, C. *et al.* RB1 loss overrides PARP inhibitor sensitivity driven by RNASEH2B loss in prostate cancer. *Sci Adv* **(in press)** (2022).
37 Saredi, G. *et al.* H4K20me0 marks post-replicative chromatin and recruits the TONSL-MMS22L DNA repair complex. *Nature* **534**, 714-718, doi:10.1038/nature18312 (2016).

38 O'Donnell, L. *et al.* The MMS22L-TONSL complex mediates recovery from replication stress and homologous recombination. *Mol Cell* **40**, 619-631, doi:10.1016/j.molcel.2010.10.024 (2010).
39 Duro, E. *et al.* Identification of the MMS22L-TONSL complex that promotes homologous recombination. *Mol Cell* **40**, 632-644, doi:10.1016/j.molcel.2010.10.023 (2010).
40 Piwko, W. *et al.* The MMS22L-TONSL heterodimer directly promotes RAD51-dependent recombination upon replication stress. *EMBO J* **35**, 2584-2601, doi:10.15252/embj.201593132 (2016).
41 How, J. A. *et al.* Modification of Homologous Recombination Deficiency Score Threshold and Association with Long-Term Survival in Epithelial Ovarian Cancer. *Cancers (Basel)* **13**, doi:10.3390/cancers13050946 (2021).
42 Telli, M. L. *et al.* Homologous Recombination Deficiency (HRD) Score Predicts Response to Platinum-Containing Neoadjuvant Chemotherapy in Patients with Triple-Negative Breast Cancer. *Clin Cancer Res* **22**, 3764-3773, doi:10.1158/1078-0432.CCR-15-2477 (2016).
43 Ray-Coquard, I. *et al.* Olaparib plus Bevacizumab as First-Line Maintenance in Ovarian Cancer. *N Engl J Med* **381**, 2416-2428, doi:10.1056/NEJMoa1911361 (2019).
44 Sztupinszki, Z. *et al.* Detection of Molecular Signatures of Homologous Recombination Deficiency in Prostate Cancer with or without BRCA1/2 Mutations. *Clin Cancer Res* **26**, 2673-2680, doi:10.1158/1078-0432.CCR-19-2135 (2020).
45 Davies, H. *et al.* HRDetect is a predictor of BRCA1 and BRCA2 deficiency based on mutational signatures. *Nat Med* **23**, 517-525, doi:10.1038/nm.4292 (2017).
46 Chappell, W. H. *et al.* p53 expression controls prostate cancer sensitivity to chemotherapy and the MDM2 inhibitor Nutlin-3. *Cell Cycle* **11**, 4579-4588, doi:10.4161/cc.22852 (2012).
47 Makvandi, M. *et al.* A PET imaging agent for evaluating PARP-1 expression in ovarian cancer. *J Clin Invest* **128**, 2116-2126, doi:10.1172/JCI97992 (2018).
48 Gogola, E. *et al.* Selective Loss of PARG Restores PARylation and Counteracts PARP Inhibitor-Mediated Synthetic Lethality. *Cancer Cell* **33**, 1078-1093 e1012, doi:10.1016/j.ccell.2018.05.008 (2018).
49 Jaspers, J. E. *et al.* Loss of 53BP1 causes PARP inhibitor resistance in Brca1-mutated mouse mammary tumors. *Cancer Discov* **3**, 68-81, doi:10.1158/2159-8290.CD-12-0049 (2013).
50 Prokhorova, E. *et al.* Unrestrained poly-ADP-ribosylation provides insights into chromatin regulation and human disease. *Mol Cell*, doi:10.1016/j.molcel.2021.04.028 (2021).
51 El Gammal, A. T. *et al.* Chromosome 8p deletions and 8q gains are associated with tumor progression and poor prognosis in prostate cancer. *Clin Cancer Res* **16**, 56-64, doi:10.1158/1078-0432.CCR-09-1423 (2010).
52 Cai, Y. *et al.* Loss of Chromosome 8p Governs Tumor Progression and Drug Response by Altering Lipid Metabolism. *Cancer Cell* **29**, 751-766, doi:10.1016/j.ccell.2016.04.003 (2016).
53 Lord, C. J. & Ashworth, A. BRCAness revisited. *Nat Rev Cancer* **16**, 110-120, doi:10.1038/nrc.2015.21 (2016).
54 Stopsack, K. H. Efficacy of PARP Inhibition in Metastatic Castration-resistant Prostate Cancer is Very Different with Non-BRCA DNA Repair Alterations: Reconstructing Prespecified Endpoints for Cohort B from the Phase 3 PROfound Trial of Olaparib. *Eur Urol* **79**, 442-445, doi:10.1016/j.eururo.2020.09.024 (2021).
55 Tung, N. M. *et al.* TBCRC 048: Phase II Study of Olaparib for Metastatic Breast Cancer and Mutations in Homologous Recombination-Related Genes. *J Clin Oncol* **38**, 4274-4282, doi:10.1200/JCO.20.02151 (2020).

814 56 Lee, J. S., Collins, K. M., Brown, A. L., Lee, C. H. & Chung, J. H. hCds1-mediated
815 phosphorylation of BRCA1 regulates the DNA damage response. *Nature* **404**, 201-204,
816 doi:10.1038/35004614 (2000).
817 57 Zhang, J. *et al.* Chk2 phosphorylation of BRCA1 regulates DNA double-strand break
818 repair. *Mol Cell Biol* **24**, 708-718, doi:10.1128/MCB.24.2.708-718.2004 (2004).
819 58 Hirao, A. *et al.* DNA damage-induced activation of p53 by the checkpoint kinase Chk2.
820 *Science* **287**, 1824-1827, doi:10.1126/science.287.5459.1824 (2000).
821 59 Takai, H. *et al.* Chk2-deficient mice exhibit radioresistance and defective p53-mediated
822 transcription. *EMBO J* **21**, 5195-5205, doi:10.1093/emboj/cdf506 (2002).
823 60 Aksoy, O. *et al.* The atypical E2F family member E2F7 couples the p53 and RB
824 pathways during cellular senescence. *Genes Dev* **26**, 1546-1557,
825 doi:10.1101/gad.196238.112 (2012).
826 61 Clements, K. E. *et al.* Loss of E2F7 confers resistance to poly-ADP-ribose polymerase
827 (PARP) inhibitors in BRCA2-deficient cells. *Nucleic Acids Res* **46**, 8898-8907,
828 doi:10.1093/nar/gky657 (2018).
829 62 Kim, H. *et al.* Combining PARP with ATR inhibition overcomes PARP inhibitor and
830 platinum resistance in ovarian cancer models. *Nat Commun* **11**, 3726,
831 doi:10.1038/s41467-020-17127-2 (2020).
832 63 Yap, T. A. *et al.* Phase I Trial of First-in-Class ATR Inhibitor M6620 (VX-970) as
833 Monotherapy or in Combination With Carboplatin in Patients With Advanced Solid
834 Tumors. *J Clin Oncol* **38**, 3195-3204, doi:10.1200/JCO.19.02404 (2020).
835 64 Ianevski, A., Giri, A. K. & Aittokallio, T. SynergyFinder 2.0: visual analytics of multi-drug
836 combination synergies. *Nucleic Acids Res* **48**, W488-W493, doi:10.1093/nar/gkaa216
837 (2020).
838 65 Ianevski, A., He, L., Aittokallio, T. & Tang, J. SynergyFinder: a web application for
839 analyzing drug combination dose-response matrix data. *Bioinformatics* **33**, 2413-2415,
840 doi:10.1093/bioinformatics/btx162 (2017).
841 66 Huang, T. H. *et al.* The Histone Chaperones ASF1 and CAF-1 Promote MMS22L-
842 TONSL-Mediated Rad51 Loading onto ssDNA during Homologous Recombination in
843 Human Cells. *Mol Cell* **69**, 879-892 e875, doi:10.1016/j.molcel.2018.01.031 (2018).
844 67 Tutt, A. N. J. *et al.* Adjuvant Olaparib for Patients with BRCA1- or BRCA2-Mutated
845 Breast Cancer. *N Engl J Med* **384**, 2394-2405, doi:10.1056/NEJMoa2105215 (2021).
846 68 Kondrashova, O. *et al.* Secondary Somatic Mutations Restoring RAD51C and RAD51D
847 Associated with Acquired Resistance to the PARP Inhibitor Rucaparib in High-Grade
848 Ovarian Carcinoma. *Cancer Discov* **7**, 984-998, doi:10.1158/2159-8290.CD-17-0419
849 (2017).
850 69 Lin, K. K. *et al.* BRCA Reversion Mutations in Circulating Tumor DNA Predict Primary
851 and Acquired Resistance to the PARP Inhibitor Rucaparib in High-Grade Ovarian
852 Carcinoma. *Cancer Discov* **9**, 210-219, doi:10.1158/2159-8290.CD-18-0715 (2019).
853 70 Pettitt, S. J. *et al.* Clinical BRCA1/2 Reversion Analysis Identifies Hotspot Mutations and
854 Predicted Neoantigens Associated with Therapy Resistance. *Cancer Discov* **10**, 1475-
855 1488, doi:10.1158/2159-8290.CD-19-1485 (2020).
856 71 Ter Brugge, P. *et al.* Mechanisms of Therapy Resistance in Patient-Derived Xenograft
857 Models of BRCA1-Deficient Breast Cancer. *J Natl Cancer Inst* **108**,
858 doi:10.1093/jnci/djw148 (2016).
859 72 Wang, Y. *et al.* BRCA1 intronic Alu elements drive gene rearrangements and PARP
860 inhibitor resistance. *Nat Commun* **10**, 5661, doi:10.1038/s41467-019-13530-6 (2019).
861 73 Wang, Y. *et al.* The BRCA1-Delta11q Alternative Splice Isoform Bypasses Germline
862 Mutations and Promotes Therapeutic Resistance to PARP Inhibition and Cisplatin.
863 *Cancer Res* **76**, 2778-2790, doi:10.1158/0008-5472.CAN-16-0186 (2016).

74 Xu, G. *et al.* REV7 counteracts DNA double-strand break resection and affects PARP inhibition. *Nature* **521**, 541-544, doi:10.1038/nature14328 (2015).
75 Noordermeer, S. M. *et al.* The shieldin complex mediates 53BP1-dependent DNA repair. *Nature* **560**, 117-121, doi:10.1038/s41586-018-0340-7 (2018).
76 Gupta, R. *et al.* DNA Repair Network Analysis Reveals Shieldin as a Key Regulator of NHEJ and PARP Inhibitor Sensitivity. *Cell* **173**, 972-988 e923, doi:10.1016/j.cell.2018.03.050 (2018).
77 Gonzalez-Billalabeitia, E. *et al.* Vulnerabilities of PTEN-TP53-deficient prostate cancers to compound PARP-PI3K inhibition. *Cancer Discov* **4**, 896-904, doi:10.1158/2159-8290.CD-13-0230 (2014).
78 Cancer Genome Atlas Research, N. Integrated genomic analyses of ovarian carcinoma. *Nature* **474**, 609-615, doi:10.1038/nature10166 (2011).
79 de Bono, J., Kang, J. & Hussain, M. Olaparib for Metastatic Castration-Resistant Prostate Cancer. Reply. *N Engl J Med* **383**, 891, doi:10.1056/NEJMc2023199 (2020).
80 Mu, P. *et al.* SOX2 promotes lineage plasticity and antiandrogen resistance in TP53- and RB1-deficient prostate cancer. *Science* **355**, 84-88, doi:10.1126/science.aah4307 (2017).
81 Ku, S. Y. *et al.* Rb1 and Trp53 cooperate to suppress prostate cancer lineage plasticity, metastasis, and antiandrogen resistance. *Science* **355**, 78-83, doi:10.1126/science.aah4199 (2017).
82 Yazinski, S. A. *et al.* ATR inhibition disrupts rewired homologous recombination and fork protection pathways in PARP inhibitor-resistant BRCA-deficient cancer cells. *Genes Dev* **31**, 318-332, doi:10.1101/gad.290957.116 (2017).
83 Decker, K. F. *et al.* Persistent androgen receptor-mediated transcription in castration-resistant prostate cancer under androgen-deprived conditions. *Nucleic Acids Res* **40**, 10765-10779, doi:10.1093/nar/gks888 (2012).
84 Gui, B. *et al.* Selective targeting of PARP-2 inhibits androgen receptor signaling and prostate cancer growth through disruption of FOXA1 function. *Proc Natl Acad Sci U S A* **116**, 14573-14582, doi:10.1073/pnas.1908547116 (2019).
85 Zheng, D. *et al.* Secretory leukocyte protease inhibitor is a survival and proliferation factor for castration-resistant prostate cancer. *Oncogene* **35**, 4807-4815, doi:10.1038/onc.2016.13 (2016).
86 Li, W. *et al.* MAGeCK enables robust identification of essential genes from genome-scale CRISPR/Cas9 knockout screens. *Genome Biol* **15**, 554, doi:10.1186/s13059-014-0554-4 (2014).
87 Li, W. *et al.* Quality control, modeling, and visualization of CRISPR screens with MAGeCK-VISPR. *Genome Biol* **16**, 281, doi:10.1186/s13059-015-0843-6 (2015).
88 Li, Y. *et al.* SRRM4 gene expression correlates with neuroendocrine prostate cancer. *Prostate* **79**, 96-104, doi:10.1002/pros.23715 (2019).
89 Dobin, A. *et al.* STAR: ultrafast universal RNA-seq aligner. *Bioinformatics* **29**, 15-21, doi:10.1093/bioinformatics/bts635 (2013).
90 Anders, S., Pyl, P. T. & Huber, W. HTSeq--a Python framework to work with high-throughput sequencing data. *Bioinformatics* **31**, 166-169, doi:10.1093/bioinformatics/btu638 (2015).
91 Love, M. I., Huber, W. & Anders, S. Moderated estimation of fold change and dispersion for RNA-seq data with DESeq2. *Genome Biol* **15**, 550, doi:10.1186/s13059-014-0550-8 (2014).
92 Subramanian, A. *et al.* Gene set enrichment analysis: a knowledge-based approach for interpreting genome-wide expression profiles. *Proc Natl Acad Sci U S A* **102**, 15545-15550, doi:10.1073/pnas.0506580102 (2005).

93 Sztupinszki, Z. *et al.* Migrating the SNP array-based homologous recombination deficiency measures to next generation sequencing data of breast cancer. *NPJ Breast Cancer* **4**, 16, doi:10.1038/s41523-018-0066-6 (2018).
94 Li, R. & Jia, Z., doi:10.1101/2021.06.29.449134 (2021).
95 Oki, S. *et al.* ChIP-Atlas: a data-mining suite powered by full integration of public ChIP-seq data. *EMBO Rep* **19**, doi:10.15252/embr.201846255 (2018).
96 Conway, J. R., Lex, A. & Gehlenborg, N. UpSetR: an R package for the visualization of intersecting sets and their properties. *Bioinformatics* **33**, 2938-2940, doi:10.1093/bioinformatics/btx364 (2017).
97 Long, Q. *et al.* Global transcriptome analysis of formalin-fixed prostate cancer specimens identifies biomarkers of disease recurrence. *Cancer Res* **74**, 3228-3237, doi:10.1158/0008-5472.CAN-13-2699 (2014).
98 Ross-Adams, H. *et al.* Integration of copy number and transcriptomics provides risk stratification in prostate cancer: A discovery and validation cohort study. *EBioMedicine* **2**, 1133-1144, doi:10.1016/j.ebiom.2015.07.017 (2015).

Acknowledgments

This work was supported by NCI R21CA252578 (to L.J.), NCI R01CA262524 (to L.J.).

Author contribution

T.Tsujino and T.Takai performed the majority of experiments and analyses. T.Tsujino and T.Takai, and K.H undertook the CRISPR screens. T.Tsujino and L.J. wrote the manuscript and prepared figures. F.G. performed animal studies. T.Tsutsumi, X.B., C.M, C.F., B.G., and A.S. performed cell studies and provided technical assistance. Z.Sztupinszki performed HRD analysis. N.X., L.F. and X.D. performed DNA scope assay. H.A. and A.S.K. provided administrative support. T.Tsujino, K.H, A.D.C., K.W.M., Z. Szallasi, L.Z., A.S.K., L.J. analyzed the data and revised manuscript. L.J. conceptualized, designed the study, and acquired funding for the present study.

Competing interests: Authors declare no competing interests.

Figure 1.

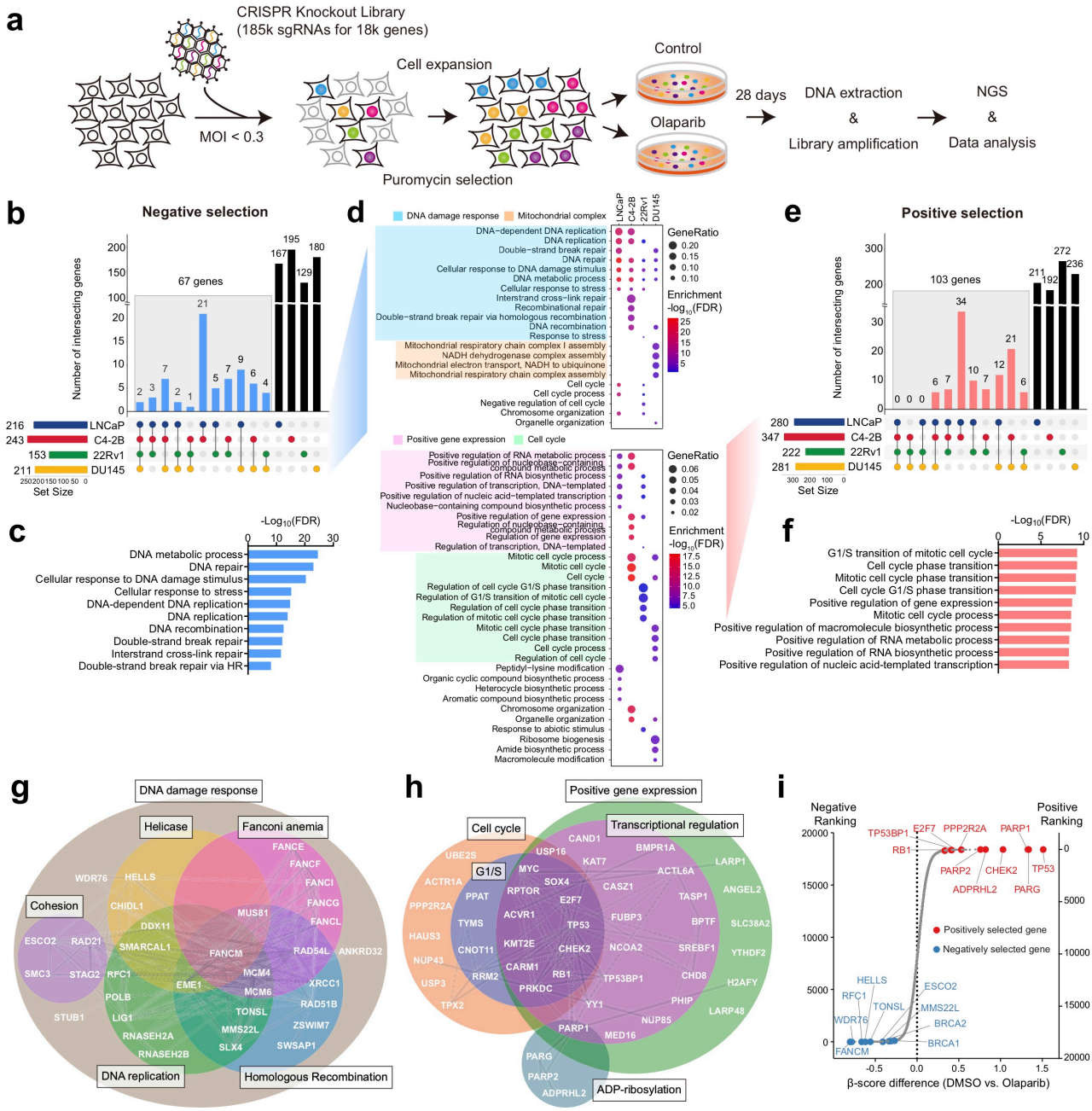

Fig. 1 CRISPR screens identify genes that modulate PARPi response in PCa cells. a, Schematic of genome-wide CRISPR/Cas9 screens. **b,** UpSet plot [96] of negatively selected genes in four PCa cell lines as indicated. Blue bars indicate the number of common hits in at least two screens. **c,** Top GO terms enriched in 67 common hits from negative selection. **d,** Top

951 GO terms enriched in negatively (upper panel) and positively (lower panel) selected genes in
952 each individual cell line. **e,** UpSet plot of positively selected genes in four PCa cell lines as
953 indicated. Red bars indicate the number of common hits in at least two screens. **f,** Top GO
954 terms enriched in 103 common hits from positive selection. **g,** The networks of common hits
955 from negative selection, grouped according to their roles in specific pathways, and their genetic
956 and physical interactions (gray lines) based on STRING analyses. **h,** The networks of common
957 hits from positive selection as described in (**g**). **i,** Top-ranked genes in CRISPR screens
958 determined by comparing olaparib treatment to DMSO treatment. Genes are ranked by the
959 average of differential β-scores from all four cell lines. Negatively and positively selected genes
960 are marked in blue and red, respectively.
961

962 **Figure 2.**

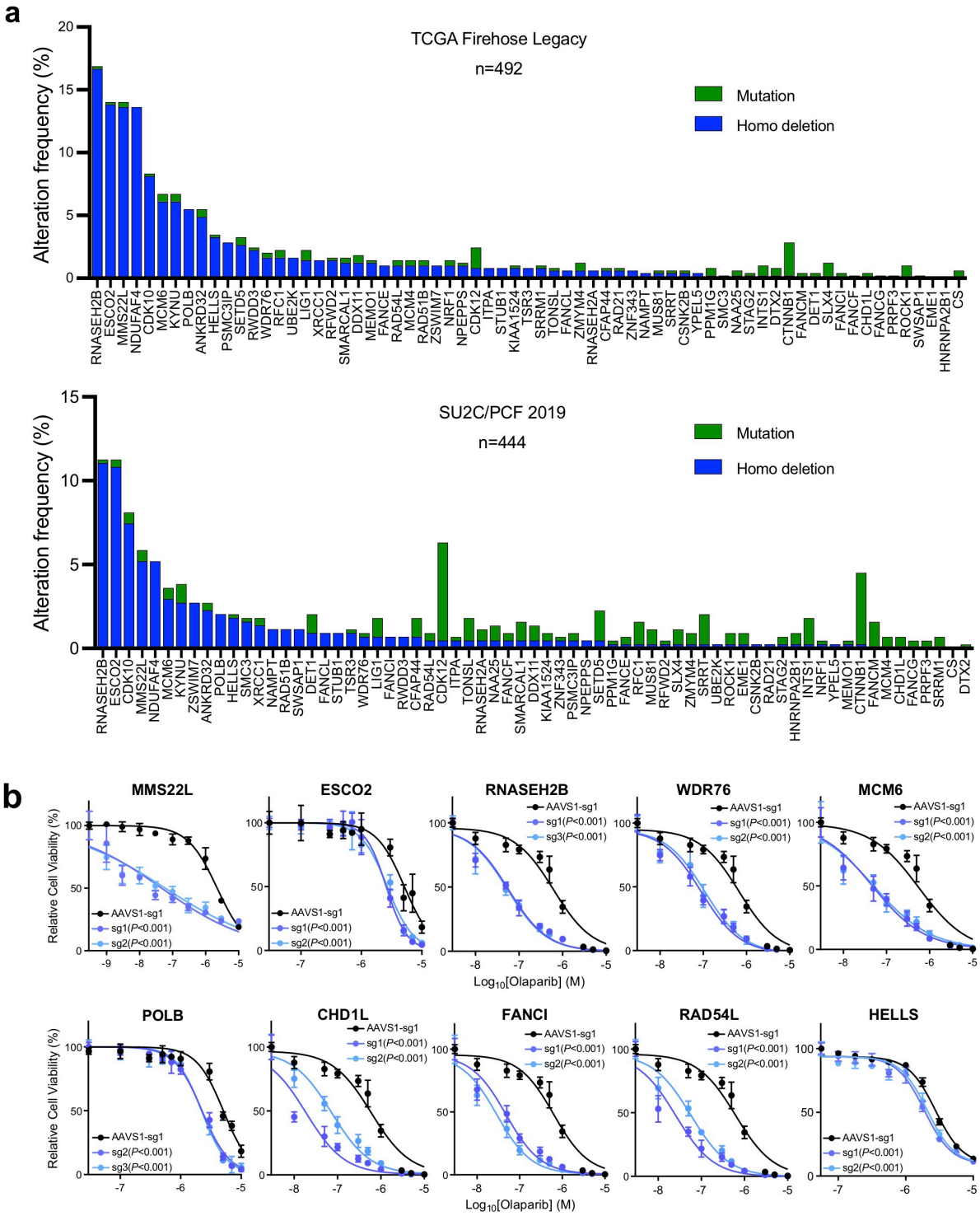

963

964 **Fig. 2 Validation of negatively selected genes with frequent genomic alterations. a,** The

965 frequency of mutations and homozygous (Homo) deletions in 67 common negatively selected

966 genes from the TCGA Firehose Legacy cohort (Upper panel, n = 492) and the SU2C/PCF
967 cohort (Lower panel, n = 444). **b,** Dose response curves after treatment with olaparib in C4-2B
968 cells with knockout (KO) of the indicated genes. The *p*-values were determined by comparing
969 two gene-specific sgRNAs to a control AAVS1 sgRNA using two-way ANOVA. Error bars
970 represent SD, n = 6.
971

Figure 3.

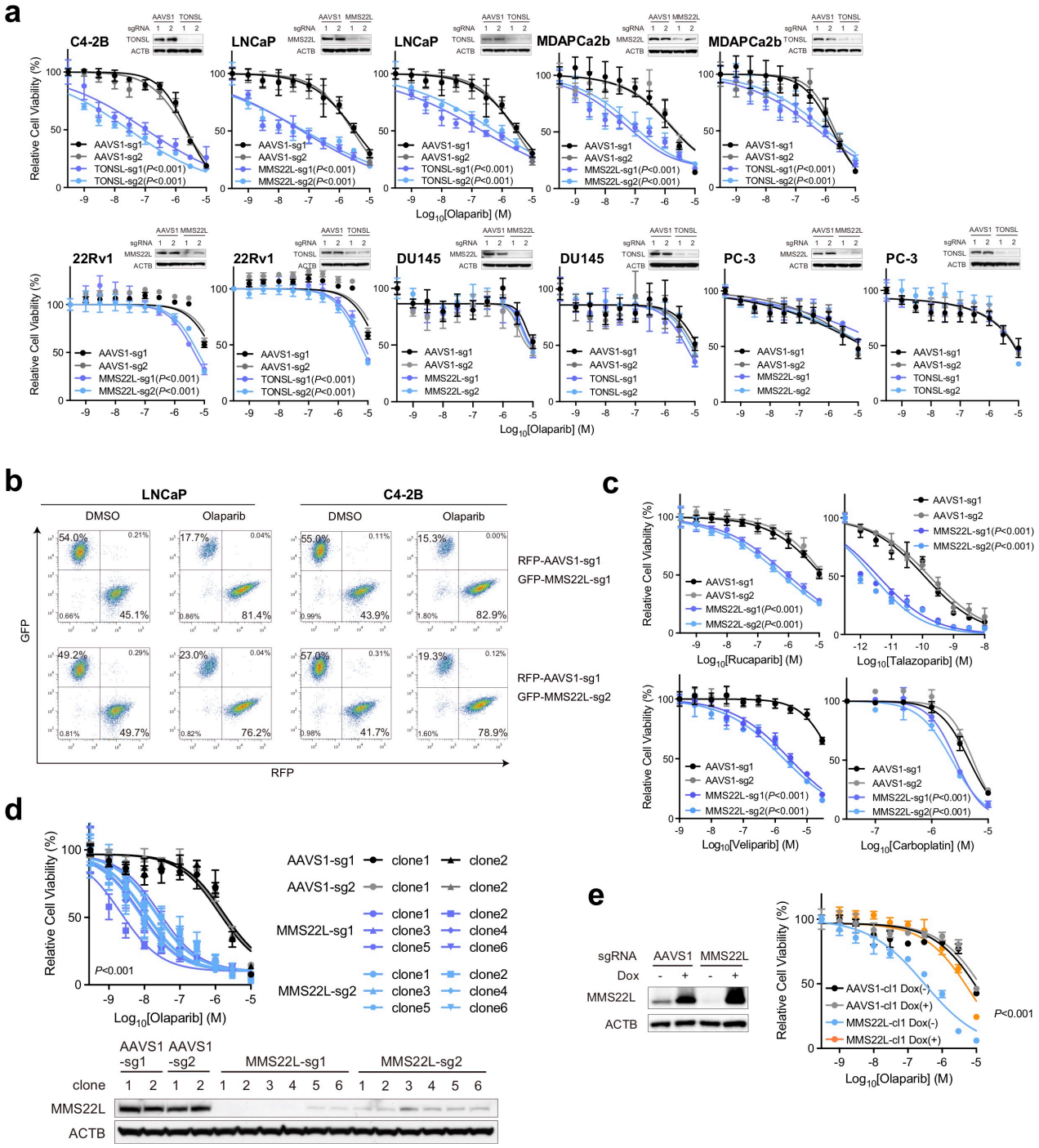

Fig. 3 Loss of MMS22L increases PARPi response in PCa cells. a, Dose response curves after treatment with olaparib in MMS22L- or TONSL-KO cells versus corresponding AAVS1 control cells of C4-2B, LNCaP, MDAPCa2b, 22Rv1, DU145 and PC-3. Upper right panels in

977 each cell line are immunoblot analysis of MMS22L or TONSL KO efficiency. ACTB (β-actin) is a
978 loading control. The olaparib response in MMS22L-KO C4-2B cells is presented in (**2b**). **b,** Flow
979 cytometry analyses of GFP and RFP positive cells. MMS22L-KO LNCaP or C4-2B cells (with
980 GFP) were co-cultured with corresponding AAVS1 control cells (with RFP) in a 1:1 ratio in the
981 presence of DMSO or olaparib (3 μM). Two MMS22L-KO cell lines (sg1 and sg2) and one
982 control cell line (sg1) were used. Cells were collected and analyzed using flow cytometry 7 days
983 after the treatment. The percentage of each cell population is presented in each panel. **c,** Dose
984 response curves after treatment with rucaparib, talazoparib, veliparib and carboplatin in two
985 MMS22L-KO C4-2B cell lines (sg1 and sg2) versus two AAVS1 control cell lines (sg1 and sg2).
986 **d,** Dose response curves (upper panel) after treatment with olaparib in control and MMS22L-KO
987 C4-2B cell clones. Immunoblot analysis (lower panel) of the MMS22L protein level in AAVS1
988 control and MMS22L-KO cell clones. **e,** Immunoblot analysis (left panel) of the MMS22L protein
989 level in C4-2B AAVS1 control sg1 clone 1 (cl1) and MMS22L-KO sg1 clone 1 (cl1), stably
990 infected with TET-inducible sgRNA-resistant MMS22L gene, after treatment with or without
991 doxycycline (0.15 μg/ml) for 3 days. Dose response curves (right panel) after olaparib treatment
992 with or without doxycycline (0.15 μg/ml) treatment in the same C4-2B cell clones. The *p*-value
993 was determined by comparison between the MMS22L-KO cell clone with and without
994 doxycycline treatment using two-way ANOVA. Error bars represent SD, n = 6. In (**a**), (**c**) and (**d**),
995 the *p*-values were determined by comparing MMS22L- or TONSL-KO cells to corresponding
996 control cells using two-way ANOVA. Error bars represent SD, n = 6.
997

Figure 4.

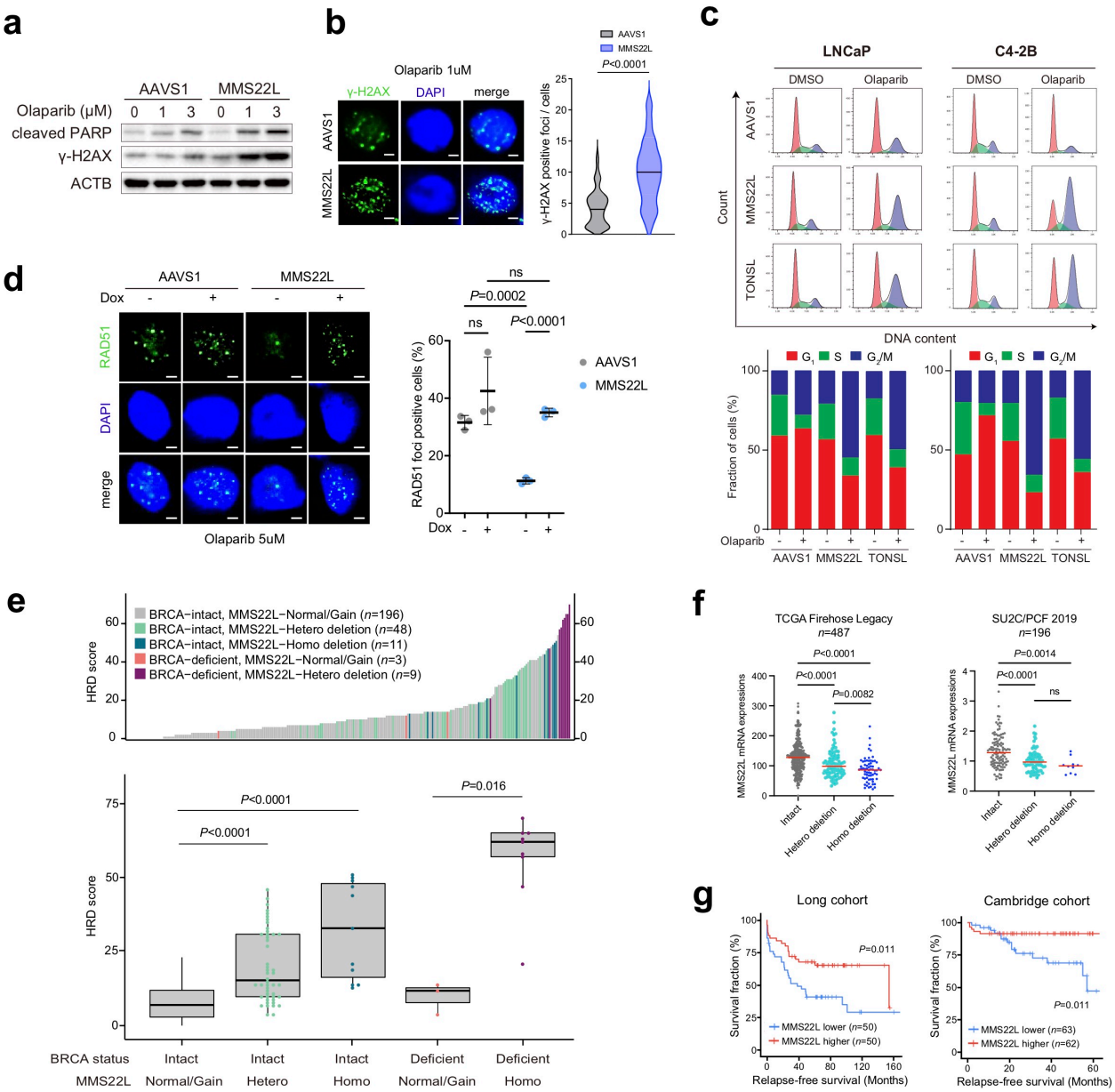

Fig. 4 Loss of MMS22L impairs HRR function in PCa cells. a, Immunoblot analysis of cleaved PARP and γ-H2AX in AAVS1 control and MMS22L-KO C4-2B cells after olaparib treatment for 72 hours with the indicated concentrations. **b,** Representative images and quantification of γ-H2AX foci in AAVS1 control and MMS22L-KO C4-2B cells after olaparib treatment (1 μM) for 24 hours. More than 100 cells were analyzed per condition. Solid lines

1005 inside the violin indicate the median. The *p*-value was determined using unpaired *t*-test. Scale
1006 bar = 5 μm. **c,** Cell cycle analysis (upper panel) in AAVS1 control, MMS22L-KO and TONSL-KO
1007 LNCaP and C4-2B cells after treatment with DMSO or olaparib (5 μM) for 72 hours. Percentage
1008 of cells (lower panel) in each phase of the cell cycle in these cells. **d,** Representative images
1009 and quantification of RAD51 foci in AAVS1 control and MMS22L-KO C4-2B cells stably infected
1010 with TET-inducible MMS22L gene after olaparib (5 μM) treatment in the presence or absence of
1011 doxycycline (0.15 μg/ml) for 24 h. Dots indicate each replicate with more than 100 cells
1012 analyzed. The *p*-values were determined using unpaired *t*-test. Error bars represent SD, n = 3.
1013 ns = not significant. Scale bar = 5 μm. **e,** Ranked HRD scores (Upper panel) in PCa tumors with
1014 BRCA and/or MMS22L genomic alterations as indicated. Comparison of HRD scores (lower
1015 panel) between patients groups classified based on BRCA and MMS22L status. HRD score is
1016 calculated using whole-genome sequencing datasets as previously described [44]. The *p*-values
1017 were determined using unpaired *t*-test. **f,** The mRNA levels of MMS22L in PCa tumors with
1018 Intact, heterozygous (Hetero) deletion and homozygous (Homo) deletion of MMS22L in the
1019 TCGA cohort (Firehose Legacy; n = 487) and the SU2C/PCF cohort (n = 196). The *p*-values
1020 were determined using unpaired *t*-test. **g,** Kaplan-Meier survival curves in the Long PCa cohort
1021 [97] and the Cambridge PCa cohort [98] based on the MMS22L mRNA expression level (lower
1022 versus higher). A log-rank test was carried out to examine the survival difference.
1023

1024 **Figure 5.**

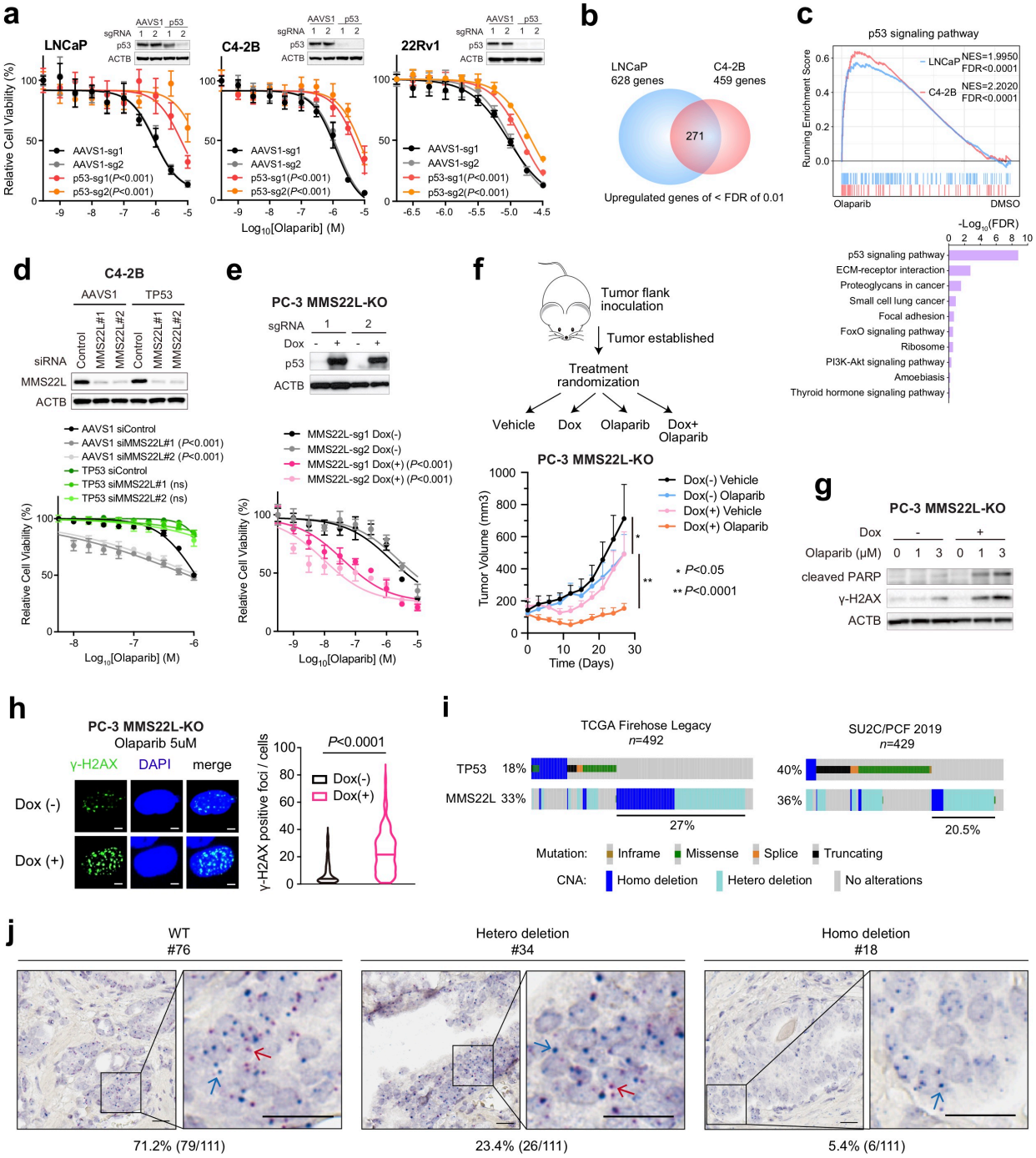

1025

1026 **Fig. 5 TP53 status impacts PARPi response in MMS22L-depleted PCa cells. a,** Dose

1027 response curves after treatment with olaparib in LNCaP, C4-2B, and 22Rv1 cells after TP53

1028 deletion. The *p*-values were determined by comparing two TP53-KO cell lines (sg1 and sg2) to

1029 two corresponding AAVS1 control cell lines (sg1 and sg2) using two-way ANOVA. Error bars
1030 represent SD, n = 6. **b,** Venn diagram of up-regulated genes in LNCaP and C4-2B cells after
1031 olaparib treatment. **c,** GSEA (upper panel) of RNA-seq data showing enrichment of p53
1032 signaling pathway in up-regulated genes in LNCaP and C4-2B after olaparib treatment. Top
1033 KEGG pathways (lower panel) enriched in these up-regulated genes. Normalized enrichment
1034 score (NES) and false discover rate (FDR) in each cell line are shown. **d,** Immunoblot analysis
1035 (upper panel) of the MMS22L protein level after siRNA knockdown. Dose response curves
1036 (lower panel) after olaparib treatment in TP53-KO and AAVS1 control C4-2B cells with or
1037 without MMS22L siRNA knockdown. Two different MMS22L siRNAs (#1 and #2) and one
1038 control siRNA were transfected into TP53-KO and control C4-2B cells for 2 days followed by
1039 olaparib treatment for 7 days. The *p*-values were determined by comparing siMMS22L to
1040 siControl using two-way ANOVA. Error bars represent SD, n = 6. **e,** Immunoblot analysis (upper
1041 panel) of p53 in AAVS1 control and MMS22L-KO PC-3 cells stably infected with TET-inducible
1042 TP53 gene in the presence or absence of doxycycline (0.15 μg/ml) for 3 days. Dose response
1043 curves (lower panel) after olaparib treatment for 7 days in the presence or absence of
1044 doxycycline (0.15 μg/ml) in these cells. The *p*-values were determined by comparing between
1045 cells treated with and without doxycycline using two-way ANOVA. Error bars represent SD, n =
1046 6. **f,** Schematic of the procedure (upper panel) in the xenograft model using MMS22L-KO PC-3
1047 cells containing TET-inducible TP53 gene. Tumor growth (lower panel) in ICR-SCID mice after
1048 treatment with olaparib (50 mg/kg) or vehicle with or without doxycycline induction for 4 weeks.
1049 The *p*-values were determined by comparing between treatment with and without doxycycline
1050 using two-way ANOVA. Error bars represent SD, n = 5. **g,** Immunoblot analysis of cleaved
1051 PARP and γ-H2AX in MMS22L-KO PC-3 cells containing TET-inducible TP53 gene after the
1052 treatment as indicated for 3 days. **h,** Representative images and quantification of γ-H2AX foci in
1053 AAVS1 control and MMS22L-KO PC-3 cells containing TET-inducible TP53 gene after olaparib

1054 (5 μM) treatment for 24 h in the presence or absence of doxycycline (0.15 μg/ml). More than
1055 100 cells were analyzed per condition. Solid lines inside the violin indicate the median. The *p*-
1056 value was determined by unpaired *t*-test. Scale bar = 5 μm. **i,** Frequency of genomic alterations
1057 in the TP53 and MMS22L genes in the TCGA cohort (left panel; Firehose Legacy, n = 492) and
1058 the SU2C/PCF cohort (right panel; n = 429). **j,** Representative images (40X) of MMS22L wild-
1059 type (WT) (sample #76), heterozygous (Hetero) deletion (sample #34), and homozygous
1060 (Homo) deletion (sample #18) determined by DNAscope using a tissue microarray (TMA)
1061 containing 146 primary prostate tumor samples. Red signals (red arrow) indicate a probe
1062 targeting the MMS22L gene on chromosome 6q. Blue signals (blue arrow) indicate a
1063 chromosome enumeration control probe targeting the centromeric region of chromosome 6p
1064 (CEP6p). The number of red and blue dots were counted and the ratio of red/blue was
1065 calculated. WT, red/blue > 0.5; Hetero deletion, red/blue between 0.1-0.5; Homo deletion,
1066 red/blue < 0.1. Scale bar = 20 μm.
1067
1068
1069

1070 **Figure 6.**

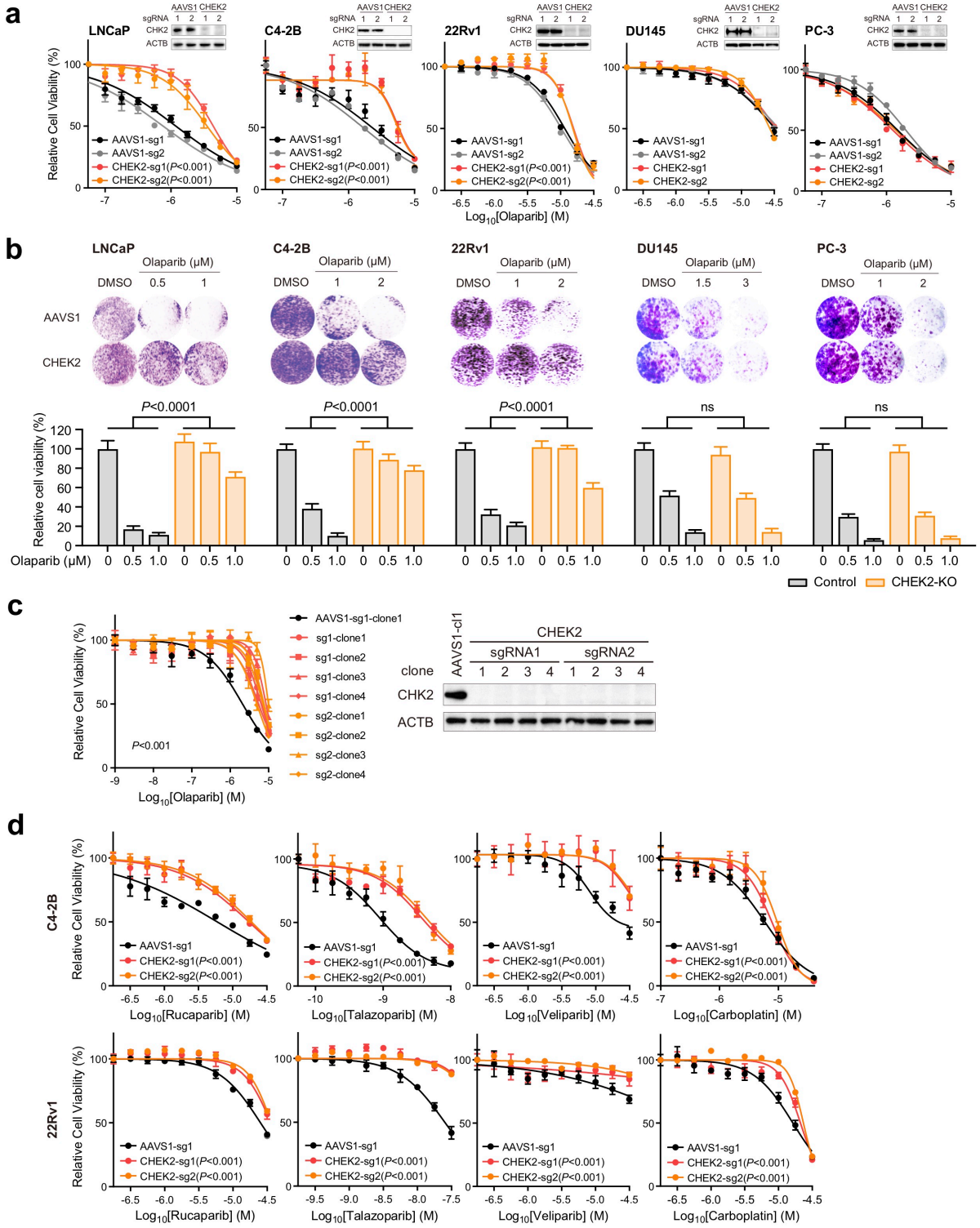

1071

1072 **Fig. 6 Loss of CHEK2 renders PCa cells resistant to PARP inhibition. a,** Dose response
1073 curves after treatment with olaparib in two CHEK2-KO (sg1 and sg2) and two AAVS1 control
1074 (sg1 and sg2) LNCaP, C4-2B, 22Rv1, DU145, and PC-3 cell lines. Upper right panel in each cell
1075 line is Immunoblot analysis of the CHEK2 protein level in CHEK2-KO versus control cells. **b,**
1076 Representative colony growth images (upper panel) and quantification (lower panel) after
1077 treatment with olaparib in CHEK2-KO and AAVS1 control PCa cell lines as indicated. The *p*-
1078 values were determined using one-way ANOVA. Error bars represent SD, n = 3. **c,** Dose
1079 response curves (left panel) after treatment with olaparib in CHEK2-KO and AAVS1 control C4-
1080 2B cell clones. Immunoblot analysis (right panel) of the CHEK2 protein level in CHEK2-KO and
1081 control cell clones. **d,** Dose response curves after treatment with rucaparib, talazoparib,
1082 veliparib and carboplatin in CHEK2-KO and AAVS1 control C4-2B and 22Rv1 cells. In (**a**), (**c**)
1083 and (**d**), the *p*-values were determined by comparing CHEK2-KO to AAVS1 control cells using
1084 two-way ANOVA. Error bars represent SD, n = 6.
1085
1086

Figure 7.

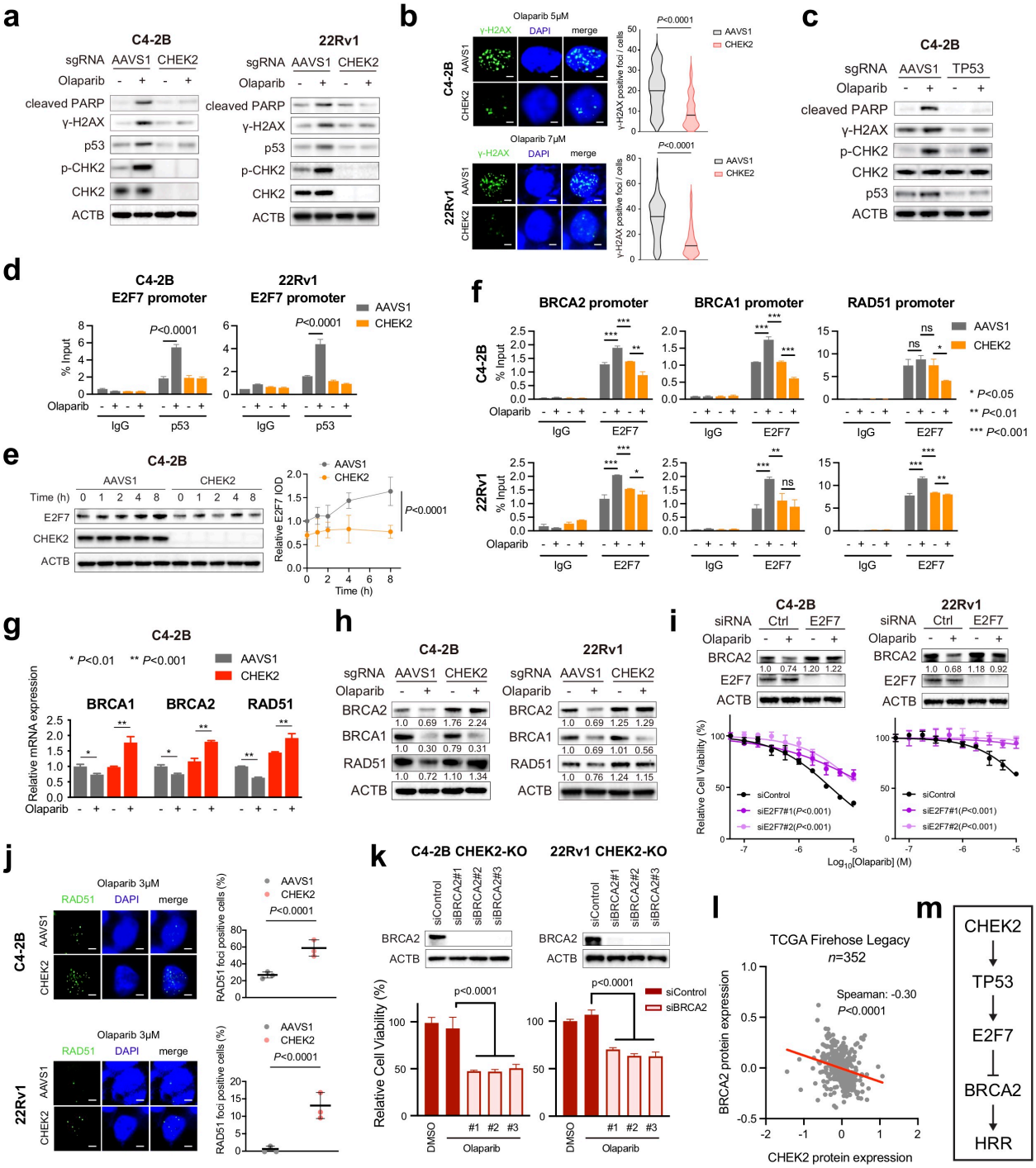

Fig. 7 Loss of CHEK2/TP53 enhances HRR function through E2F7-controlled BRCA2 expression. a, Immunoblot analysis of the indicated proteins in CHEK2-KO and AAVS1 control C4-2B and 22Rv1 cells after treatment with and without olaparib (3 μM for C4-2B and 5 μM for

1092 22Rv1) for 72 h. **b,** Representative images (left panel) and quantification (right panel) of γ-H2AX
1093 foci in CHEK2-KO and AAVS1 control C4-2B and 22Rv1 cells after treatment with olaparib (5
1094 μM for C4-2B and 7 μM for 22Rv1) for 24 h. More than 100 cells were analyzed per condition.
1095 Solid lines inside the violin indicate the median. The *p*-values were determined using unpaired *t*-
1096 test. Scale bar = 5 μm. **c,** Immunoblot analysis of the indicated proteins in TP53-KO and AAVS1
1097 control C4-2B cells after treatment with and without olaparib (3 μM) for 72 h. **d,** p53 ChIP-qPCR
1098 at the E2F7 promoter in CHEK2-KO and AAVS1 control C4-2B and 22Rv1 cells after treatment
1099 with or without olaparib (10 μM) for 24 h. **e,** Immunoblot analysis (left panel) of the E2F7 protein
1100 level in CHEK2-KO and AAVS1 control C4-2B cells after treatment with olaparib (10 μM) for the
1101 indicated time. Quantitative evaluation of integrated optical density (IOD) (right panel) was
1102 performed from three independent experiments. The E2F7 IOD values were normalized by
1103 ACTB IOD. The results are shown as mean of each time point. The *p*-values were determined
1104 by comparing CHEK2-KO to control cells using two-way ANOVA. Error bars represent SD, n=3.
1105 **f,** E2F7 ChIP-qPCR at the promoter regions of BRCA1/2 and RAD51 genes in CHEK2-KO and
1106 AAVS1 control C4-2B and 22Rv1 cells after treatment with or without olaparib (10 μM) for 24 h.
1107 **g,** The mRNA expression of BRCA1/2 and RAD51 genes determined by RT-qPCR in CHEK2-
1108 KO and AAVS1 control C4-2B cells after treatment with and without olaparib (10 μM) for 8 h. **h,**
1109 Immunoblot analysis of the indicated proteins in CHEK2-KO and AAVS1 control C4-2B and
1110 22Rv1 cells after treatment with and without olaparib (10 μM) for 72 h. The IOD values of the
1111 indicated proteins normalized by ACTB IOD are shown. **i,** Immunoblot analysis (upper panel) of
1112 BRCA2 expression in C4-2B and 22Rv1 cells after knockdown of E2F7 through RNA
1113 interference with or without olaparib (3 μM) treatment for 72 h. Two E2F7 siRNAs and one
1114 negative control (Ctrl) siRNA were used (also see Fig. 16). Dose response curves (lower panel)
1115 after treatment with olaparib for 7 days in C4-2B and 22Rv1 cells transfected with siRNAs
1116 against E2F7 or control. The *p*-values were determined by comparing siE2F7 to siControl using

1117 two-way ANOVA. Error bars represent SD, n = 6. **j,** Representative images and quantification of
1118 RAD51 foci in CHEK2-KO and AAVS1 control C4-2B cells after treatment with olaparib (3 μM)
1119 for 24 h. Dots indicate each replicate with more than 100 cells analyzed. n = 3. Scale bar = 5
1120 μm. **k,** Cell viability after treatment with olaparib (1 μM) for 7 days in CHEK2-KO C4-2B and
1121 22Rv1 cells transfected with siRNAs against BRCA2 or control. n = 6. Immunoblot analysis of
1122 the BRCA2 protein level after siRNA knockdown (upper panel). **l,** The correlation between
1123 CHEK2 and BRCA2 protein levels in the TCGA cohort (Firehose Legacy; n = 352). Spearman
1124 correlation is calculated. **m,** Schematic model of HRR function regulated by the CHEK2-TP53-
1125 E2F7-BRCA2 pathway. In (**d**), (**f**), (**g**), (**j**) and (**k**), the *p*-values were determined using unpaired
1126 *t*-test. Error bars represent SD. * $p<0.05$, ** $p<0.01$, *** $p<0.001$, ns= not significant.
1127
1128

1129 **Figure 8.**

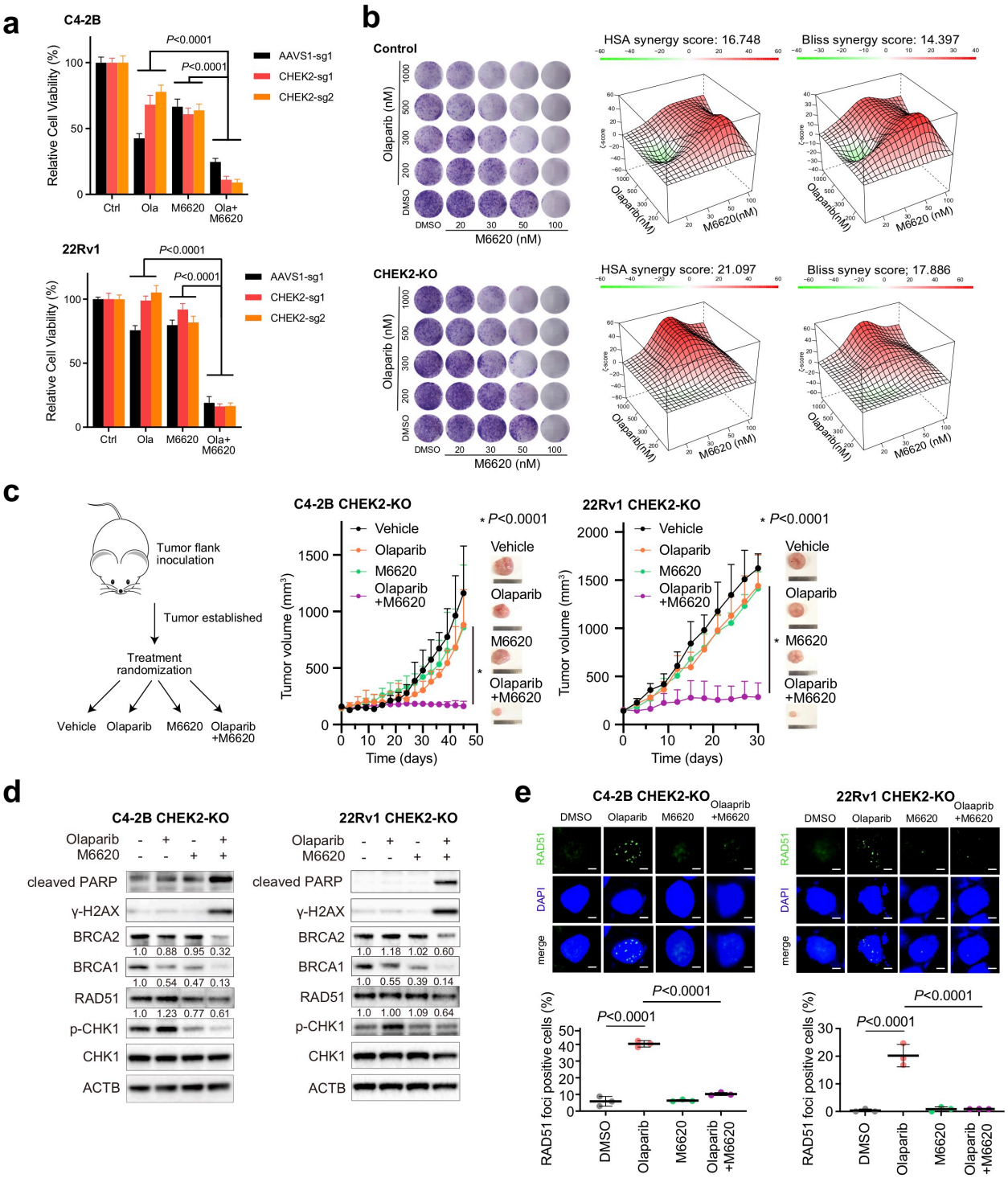

1130

1131 **Fig. 8 ATR inhibition overcomes PARPi resistance caused by CHEK2 loss in PCa cells. a,**

1132 Cell viability in CHEK2-KO and AAVS1 control C4-2B and 22Rv1 cells after treatment with

1133 DMSO, olaparib (3 μM), M6620 (100 nM) or combination of olaparib and M6620. The *p*-values
1134 were determined using one-way ANOVA. Error bars represent SD, n = 6. **b,** Representative
1135 colony growth images (left panel) after combination treatment of olaparib and M6620 in CHEK2-
1136 KO and AAVS1 control C4-2B cells. 3D synergy maps (right panel) of HSA and Bliss scores
1137 between olaparib and M6620. **c,** Schematic of the procedure (left panel) in xenograft mouse
1138 models using CHEK2-KO C4-2B and 22Rv1 cells. After tumors developed to a volume of
1139 around 150 mm^3, mice were randomized into 4 treatment groups as vehicle, olaparib (50
1140 mg/kg), M6620 (25 mg/kg) and olaparib plus M6620. The single agent was administered 5
1141 days/week, while the combination treatment was given 5 days/week for olaparib plus 4
1142 days/week for M6620. Tumor growth of CHEK2-KO C4-2B (middle panel) and 22Rv1 (right
1143 panel) cells in ICR-SCID mice treated as indicated are shown with representative images. * $p <$
1144 0.0001 was determined using two-way ANOVA. Error bars represent SD, n = 4. **d,** Immunoblot
1145 analyses of the indicated proteins in CHEK2-KO C4-2B and 22Rv1 cells after treatment as
1146 indicated (olaparib, 3 μM; M6620, 100 nM) for 72 h. The IOD values of the indicated proteins
1147 normalized by ACTB IOD were shown. **e,** Representative images (upper panel) and
1148 quantification (lower panel) of RAD51 foci in CHEK2-KO C4-2B and 22Rv1 cells after treatment
1149 as indicated (olaparib, 10 μM; M6620, 200 nM) for 24 h. Dots indicate each replicate with more
1150 than 100 cells analyzed. The *p*-values were determined using unpaired *t*-test. Error bars
1151 represent SD, n = 3. Scale bar = 5 μm.
1152